Modeling the angular correlation function and its full covariance in Photometric Galaxy Surveys

Martín Crocce[1], Anna Cabré[2] & Enrique Gaztañaga[1]

[1] *Institut de Ciències de l'Espai, IEEC-CSIC, Campus UAB, Facultat de Ciències, Torre C5 par-2, Barcelona 08193, Spain*
[2] *Center for Particle Cosmology, University of Pennsylvania, 209, South 33rd Street, Philadelphia, PA, 19104, USA*

4 July 2011

ABSTRACT

Near future cosmology will see the advent of wide area photometric galaxy surveys, like the Dark Energy Survey (DES), that extent to high redshifts ($z \sim 1-2$) but with poor radial distance resolution. In such cases splitting the data into redshift bins and using the angular correlation function $w(\theta)$, or the C_ℓ power spectrum, will become the standard approach to extract cosmological information or to study the nature of dark energy through the Baryon Acoustic Oscillations (BAO) probe. In this work we present a detailed model for $w(\theta)$ at large scales as a function of redshift and bin width, including all relevant effects, namely nonlinear gravitational clustering, bias, redshift space distortions and photo-z uncertainties. We also present a model for the full covariance matrix characterizing the angular correlation measurements, that takes into account the same effects as for $w(\theta)$ and also the possibility of a shot-noise component and partial sky coverage. Provided with a large volume N-body simulation from the MICE collaboration we built several ensembles of mock redshift bins with a sky coverage and depth typical of forthcoming photometric surveys. The model for the angular correlation and the one for the covariance matrix agree remarkably well with the mock measurements in all configurations. The prospects for a full shape analysis of $w(\theta)$ at BAO scales in forthcoming photometric surveys such as DES are thus very encouraging.

1 INTRODUCTION

The statistical analysis of the distribution of structure at large astronomical scales has played a key role in advancing the field of Cosmology over the last 20 years. From shaping our understanding of complex processes driving galaxy formation and evolution to constraining the energy density content of the Universe.

The completion of large extra-galactic surveys such at the Sloan Digital Sky Survey (SDSS, York et al. 2000) and the 2dF Galaxy Redshift Survey (2dFGRS, Colless et al. 2003) have bolstered our general knowledge in the field. Particularly more so when combined with the precise measurements of the Cosmic Microwave Background or the increasingly reach data from Supernova data (Sánchez et al. 2009; Percival et al. 2010; Reid et al. 2010; Komatsu et al. 2010) . One of the most promising, and eventually rewarding, challenges for the field of large scale structure today is the prospect for determining what drives the late time acceleration of the Universe (Riess et al. 1998; Perlmutter et al. 1999). This is probed by the presence, in the clustering pattern of galaxies, of remanent features from the cou-

pling of baryon and photons prior to recombination known as the Baryon Acoustic Oscillations (BAO). The BAO have already been detected in the spectroscopic samples of Luminous Red Galaxies (LRGs) in both SDSS and 2dFGRS (Cole et al. 2005; Eisenstein et al. 2005), and studied in the early imagining data of SDSS (Padmanabhan et al. 2007).

But the observational quest has only started. Several of the next-generation surveys will gain in area and depth, in exchange for a poorer determination of radial positions. In turn this imposes the need for angular clustering analysis in redshift bins of width few times larger that of the photometric error uncertainty at the given redshifts. The difficulty lies in that the projection in redshift bins lowers the clustering amplitude, erasing any particular feature and increasing the noise-to-signal ratio. The achievable precision of our photometrically estimated redshift will play a crucial role. We thus need to understand what affects the angular clustering pattern more severely.

The aim of our work is to tackle this problem, providing a well calibrated model for the clustering signal at large-scales as a function of angle, radial distance and bin width, deepening the available literature in the subject (e.g.

Padmanabhan et al. 2007, Blake et al. 2007 and references therein). We put particular effort in stressing the most relevant effects and their interplay, redshift distortions and photo-z uncertainties.

An equally important problem is to have the capability of estimating the full errors of the measurements. We thus provide a well tested description of the complex error matrix characterizing the measurements of the correlation function in real situations, i.e. including effects of partial sky coverage, photo-z, redshift distortions, bias and shot-noise.

Both, the model for the correlation and the one for the error matrix, will be extensively tested against a very rich set of mocks redshift bins. This work should therefore be relevant for ongoing projects that use photometric redshift estimates like the Dark Energy Survey[1] (DES), the Physics of the Accelerating Universe collaboration[2] (PAU) and the the Panoramic Survey Telescope and Rapid Response System[3] (PanStarrs). But also for upcoming imaging proposals such as the Large Synoptic Survey Telescope[4] (LSST) and the ESA/Euclid[5] survey.

This paper is organized as follows. In Sec. 2 and Sec. 3 we discuss the models proposed in this work for the angular correlation function and its full error matrix respectively. In Sec. 4 we describe the rich set of mock redshift bins ensembles implemented using a large volume N-body simulation. In Sec. 5 and 6 we test the models against the mocks, under different regimes and assumptions. Section 7 contains our conclusions and future lines of research. We also include several appendixes. In Appendix A we give a description of our model for the 3-d nonlinear matter correlation function. In Appendix B we study the limitations of the widely used Limber approximation. Finally, Appendix C gives a brief note on the covariance of the angular power spectrum induced by partial sky coverage.

2   A MODEL FOR THE ANGULAR CORRELATION FUNCTION

Let us start by considering the projection of the spatial fluctuations $\delta(\mathbf{x}, z)$ along a given direction in the sky $\hat{\mathbf{n}}$

$$\delta(\hat{\mathbf{n}}) = \int dz\, \phi(z)\, \delta(\hat{\mathbf{n}}, z), \qquad (1)$$

where ϕ is the radial selection function. The angular correlation function is then obtained as a simple projection of the 3-d correlation function ξ (Peebles 1973),

$$
\begin{aligned}
w(\theta) &\equiv \langle \delta(\hat{\mathbf{n}})\delta(\hat{\mathbf{n}} + \hat{\theta}) \rangle = \\
&= \int dz_1\, \phi(z_1) \int dz_2\, \phi(z_2)\, \xi(r_1, r_2, \theta) \qquad (2)
\end{aligned}
$$

where θ is the angle between directions $\hat{\mathbf{n}}$ and $\hat{\mathbf{n}} + \hat{\theta}$, related to the pair-separation through

$$r_{12}(\theta) = \left\{ r(z_1)^2 + r(z_2)^2 - 2r(z_1)r(z_2)\cos(\theta) \right\}^{1/2} \qquad (3)$$

and $r(z)$ is the co-moving distance to redshift z given by

$$r(z) = \int_0^z \frac{c}{H(u)} du, \qquad (4)$$

where $H(z)/H_0 = \sqrt{\Omega_m(1+z)^3 + \Omega_{DE}(1+z)^{3(1+w)}}$ is the Hubble parameter, Ω_m and $\Omega_{DE} = 1 - \Omega_m$ are the matter and dark energy densities respectively, and w is the dark energy equation of state [6].

Since we are interested in redshift bins and not in extended selections we can neglect the growth evolution and simply evaluate the 3-d correlation in some fiducial redshift (e.g. the mean redshift of the bin, weighted by ϕ). Alternatively, one can consider weighting the correlation by a linear growth $D(z)$ defined with respect to the fiducial value $\bar{z}$.

In addition, we will assume a *local and linear bias* relation between fluctuations in the tracer (e.g. galaxies) and matter density field, $\delta_g = b(z)\delta$. Under these assumptions Eq. (2) is trivially converted to

$$w(\theta) = \int dz_1\, f(z_1) \int dz_2\, f(z_2)\, \xi(r_1, r_2, \theta, \bar{z}) \qquad (5)$$

where $f(z) = D(z)\, b(z)\, \phi(z)$ and ξ is the matter 3-d correlation function.

Hence, in order to predict $w(\theta)$ we need a model for the spatial clustering accurate in a sufficiently large range of scales to allow the projection in Eq. (5), in particular when photo-z errors broadens the extent of the radial distribution.

In what follows we discuss how to include photo-z effects and the model for spatial clustering that we will use throughout this paper.

2.1   Photo-z

We incorporate the way uncertainties in the true redshift positions obtained from photometric estimates affect angular clustering by means of the radial selection function, following Budavari et al. 2003 (see also Ma et al. 2006).

The radial selection ϕ is the probability to include a galaxy in our redshift bin. If the selection of objects is done according to their true redshifts, then ϕ is equal to the true number of galaxies per unit redshift times a window function W encoding selection characteristics (e.g. redshift cuts),

$$\phi(z) = \frac{dN_g}{dz}\, W(z). \qquad (6)$$

Instead, if the selection is done according to photometric redshift estimates, one must incorporate the probability $P(z|z_p)$ for the true redshift to be z when the photometric one is z_p. The ending result is the product (Budavari et al. 2003),

$$\phi(z) = \frac{dN_g}{dz} \int dz_p\, P(z|z_p) W(z_p), \qquad (7)$$

where $W(z_p)$ is the photometric redshift window function. Throughout this paper we will only consider top-hat window functions both in true and photometric redshifts (i.e. $W = 1$ within a given redshift range, and 0 otherwise). In addition we will only consider the idealized case where the photometric estimate is Gaussianly distributed around the true redshift (e.g. Ma et al. 2006). Although this might be far from reality, it serves as an interesting starting point for more realistic scenarios (Hearin et al. 2010; Bernstein & Huterer 2010). Lastly, we recall that ϕ should be normalized to unity within the redshift range of interest.

2.2 Spatial clustering and redshift evolution

We now turn into the discussion of the 3-d matter correlation model accounting for *nonlinear gravitational effects*, *redshift space distortions*, and the way we evolve it with redshift. We postpone to Appendix A the testing of this model against measurements of 3-d matter clustering in N-body simulations.

The linear evolution of the clustering pattern preserves its shape but increases the overall amplitude. The main effects due to nonlinear gravitational clustering at large scales are a smoothing of the BAO wiggles and a rise in clustering amplitude above linear values towards smaller scales due to mode-coupling effects (Seo & Eisenstein 2005; Eisenstein et al. 2007; Crocce and Scoccimarro 2008). Although these processes can be modeled from first principles (Crocce and Scoccimarro 2006a; Matarrese & Pietroni 2008; Matsubara 2008; Taruya et al. 2009), it is also possible and desirable to find simpler parametric approximations. In the correlation function these two effects can be parameterized as (Crocce and Scoccimarro 2008),

$$\xi(r) = [\xi_{\text{Lin}}(r) \otimes e^{-(r/s_{bao})^2}](r) + A_{mc}\, \xi_{\text{Lin}}^{(1)}(r)\, \xi'_{\text{Lin}}(r) \quad (8)$$

where s_{bao} and A_{mc} are fitting parameters, ξ_{Lin} is the linear correlation function at the given redshift, ξ'_{Lin} its derivative and

$$\xi_{\text{Lin}}^{(1)} \equiv \hat{r} \cdot \nabla^{-1} \xi_{\text{Lin}}(r) = 4\pi \int P_{\text{Lin}}(k,z)\, j_1(k\,r) k\, dk. \quad (9)$$

This model have been already used in the analysis of matter, halo and galaxy clustering (Sánchez et al. 2008; Sánchez et al. 2009).

However the standard approach for analyzing clustering data in a photometric redshift survey covering from low ($z \sim 0.2$) to high redshift ($z \sim 1.4$) is to divide the data into several redshift bins (whose minimum width are ultimately determined by the photo-z accuracy, e.g. Padmanabhan et al. 2007). If one then performs a joint analysis of all these bins it is desirable to have the least number of nuisance parameters possible in order to optimize constraints on derived cosmological parameters. From this point of view it is interesting to investigate to what extent a single set of best-fit parameters can be used to describe the 3-d clustering from low to high redshift, and hence the angular clustering after the projection in Eq. (5).

We implement this as follows. The first term in Eq. (8) is proportional to the linear correlation, therefore it scales with the growth factor squared $\sim D^2(z)$. The second term arises from leading order mode-mode coupling and thus scales as $\sim D^4(z)$. In turn the damping of BAO is proportional to the amplitude of large-scale velocity flows, Eq. (A1), and so $s_{bao} \sim D(z)$. Putting these considerations together we scale our parametric model with redshift as,

$$
\begin{aligned}
\xi(r,z) &= D(z)\left[\xi_{\text{Lin},0}(r) \otimes e^{-(r/D(z)s_{bao})^2}\right](r) \\
&+ A_{mc}\, D^4(z)\, \xi_{\text{Lin},0}^{(1)}(r)\, \xi'_{\text{Lin},0}(r) \quad (10)
\end{aligned}
$$

where sub-script 0 means (linear) quantities evaluated at $z = 0$. The values for s_{bao} and A_{mc} can be taken from a best-fit analysis to $\xi(r)$ at any given redshift (or to $w(\theta)$ in any given redshift bin, after the projection in Eq. (5)). In our case will be those from the best-fit at $z = 0.3$, $s_{bao} = 6.37\, h^{-1}\,\text{Mpc}$ and $A_{mc} = 1.55$. This is detailed in Appendix A, where we present a detailed comparison of our model against numerical simulations, with particular emphasis on the scaling introduced in Eq. (10).

Lastly, we move to the inclusion of redshift space distortions. The true distance to a galaxy differs from the one derived from its redshift through the Hubble law because of the radial peculiar velocity of the galaxy on top of the Hubble flow (Kaiser 1987). At large scales, the coherent infall of galaxies into large overdensities, such as clusters, make their observed radial separation smaller, squashing the structure along the line-of-sight and boosting the amplitude of the 3-d two point correlation. In this way for separations along the line of sight $\pi \lesssim 40\, h^{-1}\,\text{Mpc}$ the correlation (or number of pairs) increases dramatically, while for larger separations the correlation becomes negative in such a way that the total number of pairs along the l.o.s is preserved (e.g. Fig. A1 in Gaztañaga et al. 2009). This implies that, by dividing the data in redshift bins, one is discarding the leverage of large radial separations effectively increasing the (angular) correlation within the bin (see Nock et al. 2010 for a recent and detailed discussion of this effect).

The linear redshift distortions discussed above, namely the Kaiser effect, can be easily described assuming the plane-parallel approximation. We will incorporate it into our modeling of the angular correlation function by writing $\xi(r_1, r_2) = \xi(\sigma, \pi)$ in Eq. (2), with (Hamilton 1992),

$$\xi(\sigma, \pi) = \xi_0(s)P_0(\mu) + \xi_2(s)P_2(\mu) + \xi_4(s)P_4(\mu), \quad (11)$$

where $\pi = r_2 - r_1$ and $\sigma^2 = 2r_1 r_2(1 - \cos\theta)$ (to yield $s = r_{12}$) are the pair-separation along and transverse to the line-of-sight, $\mu = \pi/s$ and P_ℓ are the Legendre polynomials. The double integrals in Eq. (2) are still performed in the r_1, r_2, variables leaving the evaluation of the radial selection functions unchanged. The monopoles of the anisotropic correlation $\xi_i(s)$ are given in Eqs. (B9,B10,B11) in terms of the 3-d monopole correlation $\xi(s)$, that we will take as the one including nonlinear gravitational effects given by Eq. (10). In Appendix B we discuss this effect in more detail, also in the context of the Limber approximation.

3   MODELING THE COVARIANCE MATRIX

An equally important aspect to the understanding of the signal in clustering analysis of galaxy surveys is the capability to estimate the corresponding errors in the measurements. This is of particular importance for analysis that use correlation functions in Configuration space because the measurements are highly correlated.

Notably there is scarce work in the literature aiming at developing analytical estimates of the covariance matrix of angular correlation functions besides the early work of Bernstein 1994, who developed an error estimate for the Landy & Szalay estimator in terms of higher order correlations.

Most "data analysis" papers have relied on subsampling techniques of the data itself , such as jack-knife, bootstrap and field-to-field variations (e.g. Ross et al. 2007; Meneux et al. 2009; Sawangwit et at. 2009). However as noted in the comprehensive work of Norberg et al. 2009 all these approaches have failings, at least in 3-d clustering, depending on the way they are implemented and the regime of scales of interest. On the other hand, projection along the line-of-sight alleviates this tension leading to a good agreement with theoretical estimates, as shown by Cabré et al. 2007 in the context of cross-correlations between galaxy and CMB maps.

In what follows we try to revert the lack of analytical work provided that we are interested on large angular scales, where nonlinear (i.e. non-Gaussian) effects are weaker and that we know how to model the signal itself. We thus concentrate in discussing how to model expected errors in angular clustering, including the effects of sampling variance, shot-noise, partial sky coverage, photo-z and redshift distortions. We put particular emphasis on the description of the full error matrix, and not only the diagonal components, and leave for further work the assessment of possible systematic effects.

Let us start by decomposing the fluctuations in the number of objects "per pixel" in the sky into spherical coordinates (Peebles 1973),

$$\delta(\hat{\mathbf{n}}) = \sum_{\ell \geq 0} \sum_{m=-\ell}^{\ell} a_{\ell m} Y_{\ell m}(\hat{\mathbf{n}}), \qquad (12)$$

where $\hat{\mathbf{n}}$ is the line-of-sight direction and $Y_{\ell m}$ the spherical harmonics. The coefficients in this expansion form the *angular power spectrum*,

$$\langle a_{\ell m} a_{\ell' m'} \rangle \equiv \delta_{\ell\ell'} \delta_{mm'} C_\ell \qquad (13)$$

that can be related to the *angular correlation function* using the Addition theorem [7] yielding,

$$w(\theta) = \sum_{\ell \geq 0} \left(\frac{2\ell + 1}{4\pi} \right) P_\ell(cos\theta) \, C_\ell \qquad (14)$$

where P_ℓ are the Legendre polynomials of degree ℓ. The covariance in the measurements of $w(\theta)$ can then be related

[7] $P_\ell(\hat{\mathbf{n}} \cdot \hat{\mathbf{n}}') = \frac{4\pi}{2\ell+1} \sum_{m=-\ell}^{\ell} = Y_{\ell m}(\hat{\mathbf{n}}) Y_{\ell m}^\star(\hat{\mathbf{n}})$

to those in C_ℓ as,

$$\mathrm{Cov}_{\theta\theta'} = \sum_{\ell,\ell' \geq 0} \left(\frac{2l+1}{4\pi} \right)^2 P_\ell(\cos\theta) P_{\ell'}(\cos\theta') \, \mathrm{Cov}_{\ell\ell'} \quad (15)$$

where

$$\mathrm{Cov}_{\theta\theta'} \equiv \langle \tilde{w}(\theta)\tilde{w}(\theta') \rangle, \qquad \mathrm{Cov}_{\ell\ell'} \equiv \langle \tilde{C}_\ell \tilde{C}_{\ell'} \rangle, \qquad (16)$$

and $\tilde{w}(\theta)$ and $\tilde{C}_\ell$ denote the estimators used for $w(\theta)$ and C_ℓ respectively. In a full sky situation, and assuming the $a_{\ell m}$ spectra are Gaussianly distributed, the $\tilde{C}_\ell$ measurements are uncorrelated, $\mathrm{Cov}_{\ell\ell'} = \mathrm{Var}(C_\ell)\delta_{\ell\ell'}$. In addition, one can estimate each ℓ power using the $2\ell + 1$ available modes,

$$\tilde{C}_\ell \equiv \frac{1}{2\ell + 1} \sum_{m=-\ell}^{\ell} a_{\ell m}^2 \qquad (17)$$

thus, $\mathrm{Var}(C_\ell) = 2\, C_\ell^2 / (2\ell + 1)$.

However a more realistic and interesting scenario is one in which the sky coverage is partial. In Cabré et al. 2007 it was shown, using Gaussian realizations of the $a_{\ell m}$ spectra, that errors in configurations space scale as $1/\sqrt{f_{sky}}$ (which, in turn, is the scaling of the available number of harmonic modes). In what follows we will assume this scaling, and compute the covariance matrix as (Dodelson 2003; Cabré et al. 2007)

$$\mathrm{Cov}_{\theta\theta'} = \frac{2}{f_{sky}} \sum_{\ell \geq 0} \frac{2\ell + 1}{(4\pi)^2} P_\ell(\cos\theta) P_\ell(\cos\theta') \, (C_\ell + 1/\bar{n})^2$$

$$(18)$$

where we have also included the standard shot-noise contribution arising in the variance of the C_ℓ estimates (Peebles 1973) ($\bar{n}$ is the number of objects per squared steradians). We remark that the assumption leading to Eq. (18) is *not* that the C_ℓ covariance remains diagonal in a partial sky survey but instead that $\mathrm{Cov}(\theta, \theta')$ can be obtained from its full sky expression by the scaling $1/f_{sky}$. We discuss this further in Appendix C.

To proceed further we thus need a model for the angular spectra. In *real space* the C_ℓ spectra are given by (see Appendix A)

$$C_{\ell,\mathrm{Exact}} = \frac{1}{2\pi^2} \int 4\pi k^2 dk P(k) \Psi_\ell^2(k) \qquad (19)$$

with,

$$\Psi_\ell(k) = \int dz \phi(z) D(z) j_\ell(kr(z)) \qquad (20)$$

Redshift space distortions are accounted for by following the same procedure that leads to the C_ℓ expression in Eq. (19) but starting from a power spectrum that includes the Kaiser effect discussed in Sec. 2.2 and Eq. B7. The final result is simply the following additive contribution to the kernel in Eq. (20) (**?**),

$$\Psi_\ell^r(k) = \beta \int dz \phi(z) D(z) \left[\frac{(2\ell^2 + 2\ell - 1)}{(2\ell + 3)(2\ell - 1)} j_\ell(kr) \right.$$

$$\left. - \frac{\ell(\ell - 1)}{(2\ell - 1)(2\ell + 1)} j_{\ell-2}(kr) - \frac{(\ell + 1)(\ell + 2)}{(2\ell + 1)(2\ell + 3)} j_{\ell+2}(kr) \right] \quad (21)$$

where $r = r(z)$. In turn, *photo-z* effects are included through the radial selection function $\phi(z)$, as discussed in Sec. 2.1.

Notice however that the expressions in Eqs. (19,20,21) are numerically expensive to evaluate due to the oscillatory behavior of $j_\ell(x)$ for $x \gg 1$. In Appendix B we discuss our own approach to perform these integrals, valid at large scales and involving the natural cut-off s_{bao} in Eq. (8).

4   SIMULATIONS AND MOCK SURVEY

This work aims at developing and testing analytical expressions for the signal, variance and co-variance of the angular correlation function $w(\theta)$ against measurements in mock catalogues of forthcoming photo-z surveys built upon N-body simulations.

Without loss of generality we thus imagine a survey covering a continuous $5000\,\deg^2$ of sky (i.e. a sky fraction $f_{\rm sky} = 1/8$), and redshift $0.2 < z < 1.4$ with a radial distribution given by,

$$dN/dz \propto (z/0.5)^2 \exp\left[-(z/0.5)^{1.5}\right]. \qquad (22)$$

We incorporate the fact that redshifts are estimated photometrically, with a mean photo-z error $\sigma_z(z)$, by studying angular clustering in redshift bins. The survey photo-z imposes a characteristic width for the bins, with the narrower value a few times larger than σ_z (e.g. Simpson et al. 2009). To remain general we take DES photo-z as a reference starting point (see Fig. 1) for defining our bins, and consider a range of different width for every given mean redshift. In addition, for some of these configurations we also introduce explicitly photometric errors and redshift space distortions. In this way, we cover a broad spectrum of scenarios, such that different surveys can be accommodated within our conclusions

In order to have a robust statistics but at the same time be representative of the above specifications we used partitions of a very large N-body simulation, named MICE7680, provided by the MICE collaboration[8]. The simulation tracked the gravitational evolution of 2048^3 dark-matter particles within a very large comoving volume of $L_{\rm box} = 7680\,h^{-1}$ Mpc using the `Gadget-2` code (Springel 2005). Initial conditions were set at $z_i = 150$ using the Zeldovich dynamics and assuming a flat LCDM cosmology with parameters $\Omega_m = 0.25$, $\Omega_\Lambda = 0.75$, $\Omega_b = 0.044$ and $h = 0.7$. In addition, the spectral tilt was set to $n_s = 0.95$ and the initial amplitude of fluctuations set to yield $\sigma_8 = 0.8$ at $z = 0$. The resulting particle mass was $3.65 \times 10^{12}\,h^{-1}\,{\rm M}_\odot$ (see Fosalba et al. 2008 and Crocce et al. 2010 for further details).

To fairly sample the range $0.2 < z < 1.4$ we select comoving outputs at the redshifts $\bar{z} = 0.3, 0.5, 0.73$ and 1.1. In each output we extract the matter and/or halo density field within spherical shells of radius equal to the comoving distance to the given redshift. In turn, to be representative of typical photo-z errors we set 4 different bin width for each $\bar{z}$, namely $\Delta z/(1 + z) = 0.03, 0.05, 0.1, 0.15$. Translated to comoving distance these bins range from 100 to $500\,h^{-1}$ Mpc

$\bar{z}$	$\Delta z/(1+z)$	$\bar{r}\,(\mathrm{Mpc}\,h^{-1})$	$\Delta r\,(\mathrm{Mpc}\,h^{-1})$	$Mocks$
0.3	0.03	845.7	102.65	1344
0.3	0.10	843.3	342.14	441
0.3	0.15	839.8	513.20	392
0.5	0.05	1345.8	178.23	324
0.5	0.10	1343.2	356.50	175
0.5	0.15	1338.7	534.83	150
0.73	0.05	1859.7	181.50	104
0.73	0.10	1856.5	363.10	96
0.73	0.15	1851.1	544.88	80
1.1	0.10	2558.2	360.07	36
1.1	0.15	2551.9	540.56	36

Table 1. *Mock catalogues.* Using comoving snapshots of a very-large N-body simulation we built several ensembles of mock redshift shells subtending a continuous 1/8 of the sky at a radial comoving distance and width given in the Table (we only list some configurations, see Fig. 1 for a full account). Notably, the statistics recovered (5th column) allows to test robustly not only the clustering signal but also the full measurement covariance.

in width. These spherical shells are restricted to have right ascension and declination in $0° - 90°$, therefore covering 1/8 of sky. Lastly, we impose the radial distribution of objects given in Eq. (22) by randomly selecting particles within each bin.

We put particular care in the way we place the shells within the cubic volume in order to have none or minimal spatial overlap between different mocks. The resulting number of mocks depends on $\bar{z}$ and $\Delta z/(1+z)$, but it ranges from tens to thousands, making these set of ensembles very suitable for error studies as well as for testing models and systematics. Table 1 includes the main characteristics for 11 of these bins, which are the ones that for concreteness we focus on in this paper (although our conclusions extend to the full set). The comparison of our 16 mock configurations with the approximate $\sigma_z(z)$ expected for DES (Banerji et al. 2008) is shown in Fig. 1.

Once the particles (or halos) are selected we build angular number density maps in the `Healpix` format with $N_{side} = 256$ (Górski et al. 1999)[9]. This N_{side} corresponds to 98304 pixels in 1/8 of sky with an angular resolution of 13.75 arc-min. In this way, and given our mass resolution $m_p = 3.65 \times 10^{12}\,h^{-1}\,{\rm M}_\odot$, we obtain mocks with $\sim 20 - 100$ galaxies per pixel (depending on the bin-width) in the low redshift bins ($z = 0.3$) and $\sim 200 - 800$ galaxies per pixel at high redshift ($z = 1.1$).

Before moving on we want to highlight the importance and uniqueness of the N-body run used throughout this work, which is confered by the combination of such a

---

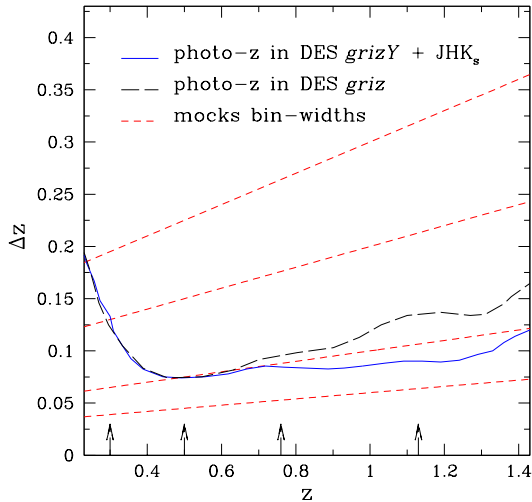[8] `http://www.ice.cat/mice`

[9] http://healpix.jpl.nasa.gov

Figure 1. *Mocks configurations* We built several ensembles of mock redshift bins covering 1/8 of sky (5000 sq deg) and with mean redshifts $\bar{z} = 0.3, 0.5, 0.73, 1.1$ (shown by the inset vertical arrows). For each $\bar{z}$ we set four different redshift width $\Delta z/(1 + z) = 0.03, 0.05, 0.1, 0.15$ (dashed lines, bottom to top respectively). The number of mocks for each configuration is given in Table I. The aim is to resemble with high statistical accuracy the geometry of large area and deep photometry galaxy surveys, such as the Dark Energy Survey (DES). The expected photo-z error in DES (using *griz* bands) is shown by the long dashed line, while the solid line shows the resulting photo-z after adding the JHK$_s$ filters from the Vista Hemisphere Survey (from Banerji et al. 2008).

large volume and adequate mass resolution. For instance, the comoving distance to $z \sim 0.5$ is $\sim 1500\,h^{-1}\,\mathrm{Mpc}$ for a concordance cosmology. Therefore, the simulation box-size needed for making just one mock at $z > 0.5$ exceeds $L_{box} \approx 1500\,h^{-1}\,\mathrm{Mpc}$. This is a serious limitation for accurate and robust statistical studies of wide and deep photo-z surveys. In our case, the simulated volume available allowed us to tackle this problem and design a mock "pipeline" that has a large potential for a number of different scientific projects other than the particular one of this paper.

5   MODEL VS. MOCKS I : THE CORRELATION SIGNAL

In Sec. 2 we discussed in detail our model for the angular correlation function. We now proceed to show how it performs against clustering measurements in the ensembles of mock redshift bins described in Sec. 4, that include the interplay of nonlinear gravitational clustering and projection effects. In addition we built some ensembles of mock z-bins using different halo samples to test the linear bias assumption for this type of tracer, as well as dark-matter mocks in photo-z and redshift space. We describe them in the sections below, together with the corresponding model comparison.

5.1   Nonlinear Gravity and evolution

Using the model for $\xi(r, z)$ in Eq. (10) we now project into redshift bins according to Eq. (5) to find the angular correlation function. The resulting correlations are shown in Fig. (2) compared with measurements in the mocks at the 4 different mean redshifts, $z = 0.3, 0.5, 0.73, 1.1$ (top to bottom). In each case for a bin width of the size of the typical photometric error achievable at the given redshift in a survey like DES (Banerji et al. 2008).

The agreement between our theoretical model and the mean of the measurements is excellent for all configurations tested, see Table 1, in particular those shown in Fig. (2). And we recall that we are using only two parameters obtained from a best-fit to ξ at $z = 0.3$ [10]. The evolution with redshift is a component of the model. In each case displayed error bars correspond to the error on the mean of the ensemble (i.e. $\sigma/\sqrt{N_{mocks}}$), that given the large number of ensemble member we count on is remarkably small.

The importance of nonlinear effects in front of projection ones are minor if we consider the large error bars achievable in one single mock measurement. It is however encouraging that one is able to model accurately a large range of angular scales, given the mixing of all the distance scales involved in the redshift bin projection.

The smaller comoving scale r_s involved in the projection of a galaxy pair subtending an angle θ within a redshift bin is given by,

$$r_c = r_{min}(z)(2 - 2\cos\theta)^{1/2} \qquad (23)$$

where $r_{min}(z)$ is the lower limit of the redshift range under consideration. A conservative approach to investigate the limitations of the model would be then to match this r_s with the minimum scale one is capable of modeling in the 3-d clustering. Interestingly we have found that, if we define r_{nl} as the scale where the model departs from the data by some fixed percentage, then our minimum scale satisfies,

$$r_{nl}(z) \sim r_{nl}(z = 0) \times D(z) \qquad (24)$$

and $r_{nl}(0) \sim 20\,h^{-1}\,\mathrm{Mpc}$ for a 15% error in ξ. This ensures the following minimal angles above which the model should perform well for the 4 cases shown in Fig. 2, $\theta_{min} = 1.3°, 0.7°, 0.5°, 0.4°$, in agreement with Fig. 2. But again, this is a conservative limit because the relative contribution of scales $\sim r_s$ to the full redshift bin projection is minor.

Lastly, we note that our mocks are *not* built from a light-cone, but rather from comoving outputs at the corresponding mean redshift $\bar{z}$, hence we do not integrate the relative growth factor as discussed prior to Eq. (5) but rather evaluate it at the given $\bar{z}$.

5.2   Biased tracers

We now revisit to what extent the possible presence of scale dependent bias in the spatial correlation function of tracers

---

[10] The level of matching does not change if we use instead the theoretical expectations for these parameter discussed in Sec. 2.2
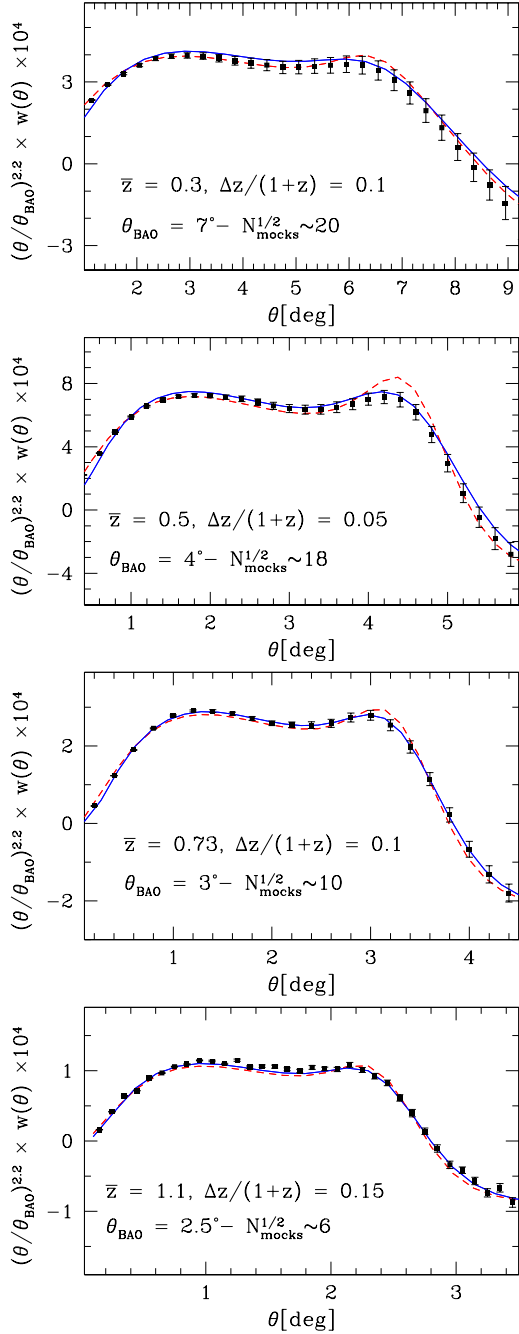
Figure 2. *Angular Correlation Function* measured in 4 ensembles of mocks z-bins compared with our nonlinear model (solid blue) and linear theory (red dashed line). Error bars correspond to the uncertainty in the mean of the ensemble, the actual r.m.s. is $N_{mock}^{1/2}$ larger (which is specified in the inset label). For each case, the width in comoving length units is given in Table 1. For concreteness we only show 4 configurations, but the agreement extends to all 16 cases. The fact that linear and nonlinear correlations coincide to the left of the bump is due to the inclusion of the mode-coupling term in our model.

(Smith et al. 2008; Manera and Gazatañaga 2009; Desjacques and Sheth 2010) translates into the angular correlation function, depending on the bin-width and mean redshift. Or equivalently, what extent the assumption of linear bias holds in the angular clustering of halos.

This test is particularly hard to implement from the numerical point of view if one desires to maintain a very good statistics as we are doing in this paper. This is because is very hard to resolve halos of $10^{12-13} \, h^{-1} \, \mathrm{M}_\odot$ in a volume as large as the one we are considering here, ~ 450 cubic Gpc/h, that allows the implementation of hundreds of mock catalogues as detailed in Sec. 4.

We concentrate in two characteristic redshifts. At $z = 0.3$ we consider groups of $M > 10^{13} \, h^{-1} \, \mathrm{M}_\odot$ (i.e. 5 or more particles) and bin width $\Delta z/(1 + z) = 0.15$. The spatial abundance of these halos is $\bar{n} = 1.7 \times 10^{-4} \, h^3 \, \mathrm{Mpc}^{-3}$. At $z = 0.5$ we consider halos with $M > 2 \times 10^{13} \, h^{-1} \, \mathrm{M}_\odot$ (8 or more particles) with $\bar{n} = 1.5 \times 10^{-4} \, h^3 \, \mathrm{Mpc}^{-3}$. With these selections we try to mimic LRG halos of $M \geq 10^{13} \, h^{-1} \, \mathrm{M}_\odot$. At $z = 0.5$ we also consider cluster mass-scale halos of $M > 10^{14} \, h^{-1} \, \mathrm{M}_\odot$ (35 particles or more), their abundance given by $\bar{n} = 0.64 \times 10^{-5} \, h^3 \, \mathrm{Mpc}^{-3}$. We do not consider bins at higher redshifts, as the galaxy bias is expected to be closer to linear and local.

The top panel of Fig. 3 shows the ratio of correlation functions (i.e. the bias) measured in the 392 mocks of $\bar{z} = 0.3$ and $\Delta z/(1 + z) = 0.15$ for halos $M > 10^{13} \, h^{-1} \, \mathrm{M}_\odot$. Middle and bottom panels shows the same ratio but from the 175 mocks bins at $z = 0.5$ and $\Delta z/(1 + z) = 0.1$ for masses $M > 2 \times 10^{13} \, h^{-1} \, \mathrm{M}_\odot$ and $M > 10^{14} \, h^{-1} \, \mathrm{M}_\odot$ respectively. For reference the vertical blue arrow shows the position of the BAO peak in each case.

In all cases the bias is scale independent well within error bars (corresponding to the mean on the ensemble) and at the $2-3\%$ level for the cases mimicking galaxy clustering ($M \sim 10^{13} \, h^{-1} \, \mathrm{M}_\odot$). For cluster mass-scale the shot-noise of the sample is much larger and consequently the error bars. Nonetheless, there is not clear tendency with scale. The error bars displayed in Fig. (3) are computed propagating the r.m.s. ensemble errors in the halo angular auto-correlation w_{hh} and the matter angular auto-correlation w as,

$$\delta b/b = (1/2) \left[(\delta w_{hh}/w_{hh})^2 + (\delta w/w)^2 \right]^{1/2} \qquad (25)$$

and converting to errors on the mean by $\delta b \to \delta b/\sqrt{N_{mocks}}$. We opted for this error estimate because the ratio of halo to matter correlation in each individual mock realization is not always positive definite, what complicates the biasing and error interpretation.

We find no evidence of scale dependence bias within the error bars.

5.3 Redshift Distortions and Photo-z

In addition to the mock ensembles described in Sec. 4 and studied in the previous section we built dedicated cases (for two of those configurations) in order to test the modeling of photo-z and redshift space distortions .
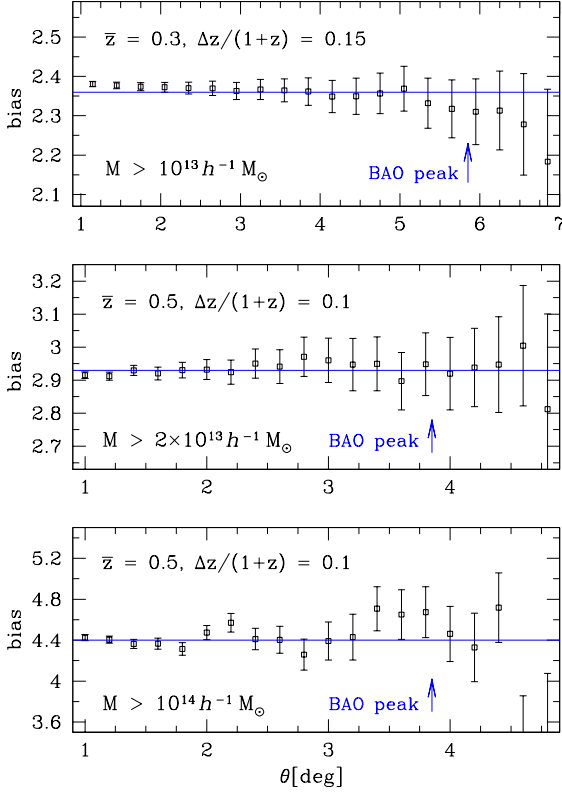
We used the comoving output of MICE7680 at $z = 0.5$

Figure 3. *Large Scale Halo Bias*, in the angular correlation function for bins at $z = 0.3$ (top panel) and $z = 0.5$ (middle and bottom). The bias is linear within few percent, and well within error bars. Except perhaps in the lower panel, that corresponds to cluster-escale mass halos with large errors fully dominated by their low abundance. See text for more details (e.g. on displayed error bars).

since this redshift is the typical mean z for upcoming photometric surveys (e.g. DES and PanStarrs). We then built ensembles of bins using top-hat selections of width $\Delta/(1+z) = 0.05$ (thin) and $\Delta/(1+z) = 0.15$ (thick), starting from either redshift or photo-z space. It total, we built 150 mocks for each of the four cases, that we discussed below.

The mapping from real **r** to *Redshift Space* positions **s** is given by the transformation

$$\mathbf{s} = \mathbf{r} + v_r(1+z)/H(z)\,\hat{\mathbf{r}} \qquad (26)$$

where H is the Hubble parameter and v_r the peculiar velocity of the object along the line of sight from the observer. Therefore given the observer at position $\mathbf{r}_0$ we first find the particle's projected velocity along the l.o.s. to the observer,

$$v_r = \frac{\mathbf{v} \cdot (\mathbf{r} - \mathbf{r}_0)}{|\mathbf{r} - \mathbf{r}_0|}, \qquad (27)$$

then displace it by $\delta r = v_r(1+z)/H(z)$ along the l.o.s.,

$$\delta\mathbf{r} = \delta r \frac{(\mathbf{r} - \mathbf{r}_0)}{|\mathbf{r} - \mathbf{r}_0|} \qquad (28)$$

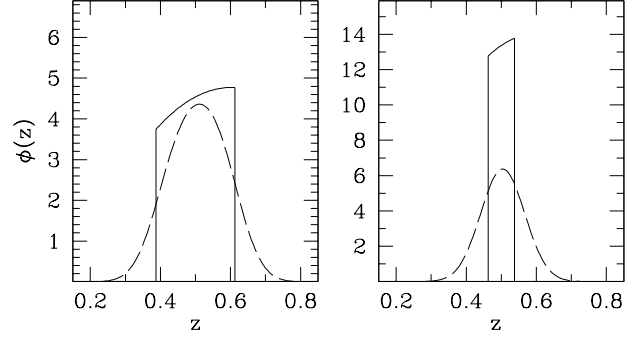and finally do the top-hat selection. We repeat this

Figure 4. *True Selection Functions in our Photo-z Mocks*. Solid lines are the radial distribution of particles for a top-hat selection in true redshift of width $\Delta z/(1+z) = 0.15$ (left panel) and $\Delta z/(1+z) = 0.05$ (right panel), both centered at $z = 0.5$ and assuming a constant spatial density. Dashed lines show the true redshift distribution after a Gaussian photometric redshift error of $\sigma_z = 0.06$ is introduced in the mocks and the same selection is done, now using photometric redshift.

procedure for each of the 150 observers within the $(7680\,h^{-1}\,\mathrm{Mpc})^3$ volume of our run.

Mocks including (Gaussian) *Photo-z* errors are produced in almost the same manner, except that the displacement along the l.o.s is random with a probability

$$f(\delta r) = \frac{1}{\sqrt{2\pi}\sigma_r} \exp\left[-\frac{\delta r^2}{2\sigma_r^2}\right] \qquad (29)$$

where $\sigma_r = \sigma_z c/H(z)$ and σ_z is the survey photometric uncertainty at the given z. We only considered $\sigma_z = 0.06$, which is the nominal value for DES at $z = 0.5$ using the griz photometric bands (Banerji et al. 2008) as reproduced our in Fig. 1. This is also the expected photo-z accuracy for the 3π all-sky survey of the Pan-Starrs collaboration (Cai et. al 2009) at this redshift using grizy bands alone. In addition, it is the approximately photo-z precision obtained for the optical sample of LRGs selected from the SDSS imaging data (Padmanabhan et al. 2005; Padmanabhan et al. 2007). This is thus a very representative value for σ_z. For our cosmology it translates to an uncertainty in the radial distance of $\sim 140\,h^{-1}$ Mpc.

Dashed line in Fig. 4 shows the real distribution of objects that entered the photo-z top-hat bins of $\Delta/(1+z) = 0.15$ (left panel) and $\Delta/(1+z) = 0.05$ (right panel) as a function of their true redshifts. This radial selection functions were obtained from Eq. (7) using the underlying distribution from Eq. (22) (shown by the solid line) and a Gaussian $P(z|z_p)$ of width $\sigma_z = 0.06$, Eq. (29). Notice that the chosen bin widths, that will be used in Figs. 5 and 7, correspond to either $\Delta \sim \sigma_z$ or $\Delta \sim 4\,\sigma_z$.

Fig. 5 corresponds to the angular correlation function measured in the mock z-bins in configuration space (middle symbols), redshif space (top symbols) and photo-z space (low symbols). In solid green, red and blue lines we show the corresponding analytical predictions obtained from Eqs. (5,7,10,B7). For redshift distortions we used that
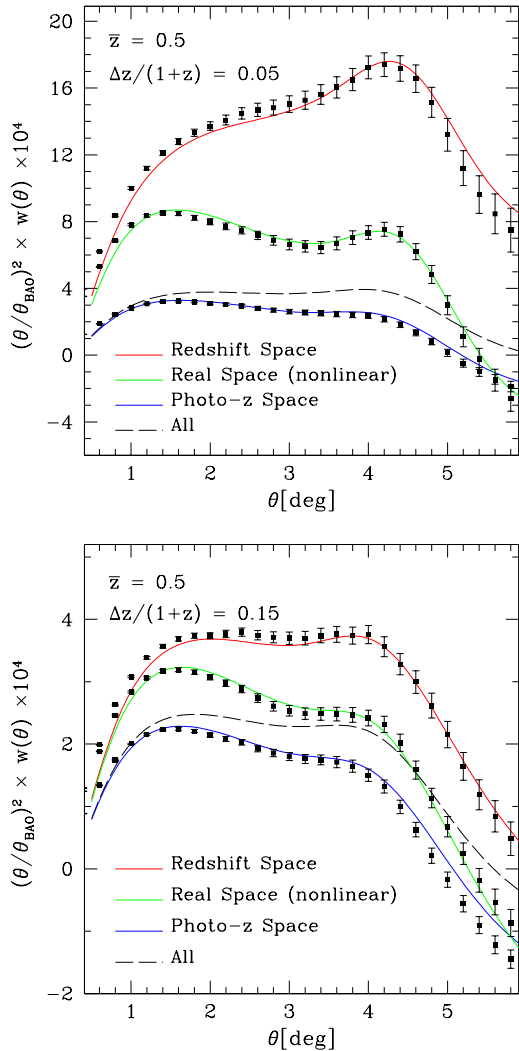
Figure 5. *Redshift Distortions and Photo-z effects: model vs. mocks.* Measurements and model of $w(\theta)$ in configuration (middle green line and symbols), redshift space (top red line and symbols) and photo-z space (low blue line and symbols). Redshift distortions (RD) depend on the parameter $\beta = f/b = 0.7047$ in this case. Photo-z errors were set to $\sigma_z = 0.06$. RD induces a strong and scale dependent enhancement of correlation, counteracted by the smearing due to the photo-z uncertainties. The final $w(\theta)$ accounting for all these effects is shown by the dashed line.

$\beta = f(z = 0.5) = 0.7047$ for our cosmology (since $b = 1$) while for photo-z we used the selection functions shown in Fig. 4. As clearly shown by Fig. 5, the model described in this paper performs remarkably well for both thin and thick bins, in configuration, redshift, and photo-z spaces.

Redshift space distortions produce a strong enhancement of the clustering signal (see (Nock et al. 2010) who find similar results for the projected correlation). This effect is also a strong function of scale, becoming more important for larger separations. Indeed, it increases the amplitude of the BAO bump by as much as a factor of 2.3 for the thin

bin of $\Delta = 0.05(1 + z) \sim 180\,h^{-1}\,\text{Mpc}$ (top panel of Fig. 5) and 1.5 for the thick one of $\Delta = 0.15(1 + z) \sim 530\,h^{-1}\,\text{Mpc}$ (bottom panel of Fig. 5).

In turn, photo-z errors have the opposite effect to that of redshift distortions, decreasing the overall amplitude of angular correlations. This is simply because the projection in Eq. (5) extends over a much larger range of scales (e.g. see Fig. 4). Notably, this effect is not far from being scale independent. For the thin bin the impact is a bit stronger (top panel of Fig. 5). If we only consider photo-z effects, the amplitude of $w(\theta)$ decreases by $\sim 60\%$ when going from true to photometric redshifts (green to blue lines in the figure). In the case of a wide bin (bottom panel in Fig. 5), although its width is approximately 4 times the photo-z and satisfies the half-width half-maximum relation with the true distribution [11], there is still a reduction in amplitude of $\sim 30\%$.

The total angular correlation, including redshift distortions, photo-z, nonlinear evolution and bin projection effects is depicted by the dashed line in Fig. 5. In the case of bin width comparable to the photo-z error the effect of photo-z dominates over redshift distortions (even though the impact of redshift distortions is larger for thinner bins). For a wider bin (bottom panel) the conjunction of effects leaves the amplitude of correlation at the BAO peak almost unchanged, but it does introduce a strong scale dependent bias with respect to the real space clustering of matter. Notably, the inclusion of redshift distortions to the $w(\theta)$ in photo-z space enhances the amplitude by up to 50% at the peak position. Clearly, the appropriate inclusion of these contributions can be crucial in the analysis of real data.

We note that the above conclusions assume an unbiased tracer. For biased ones the impact of redshift distortions, sensitive to f/b, is smaller. For instance, if we take $b = 1.7$ at $z = 0.5$, that is a characteristic value for optically selected LRGs (Padmanabhan et al. 2007; Ross et al. 2007), but keep the same σ_z we find the amplitude of $w(\theta)$ at the BAO peak position ($\theta \sim 4°$) reduced by $\sim 10\%$ with respect to the $b = 1$ case, for a bin $\Delta \sim 4 \times \sigma_z$ (but still gives 30% boost with respect to the case where redshift distortions is neglected all together).

6 MODEL VS. MOCKS II : THE ERROR MATRIX

We now move to test the performance of Eq. (18) in evaluating the full covariance matrix in $w(\theta)$ measurements. We first discuss the diagonal component, or variance, in Sec. 6.1 and then the reduced covariance in Sec. 6.2.

6.1 Comparing the $w(\theta)$ variance

In Fig. 6 we show the r.m.s dispersion resulting from $w(\theta)$ measurements in several ensembles of mock redshift bins (top panels corresponds to *narrow* bin cases, bottom to their *wide* counterpart). The total number of measurements in

---

[11] that is, the top-hat redshift limits corresponding to the values where the true distribution drops by $1/2$

each ensemble depends on the particular value of mean red-shift and width of the bin (as detailed in Table 1), but they lay in the $100 - 1000$ range, thus giving a unique statistical framework for our analysis. We stress that these mocks are obtained from comoving outputs of an N-body simulation and thus contain all correlations induced by non-linear gravitational evolution and projection effects, in addition to partial sky coverage and survey selection function. The bin selection was top-hat in true redshift in all cases (see below for photo-z and redshift space considerations) Solid lines in Fig. 6 corresponds to the prediction for the error,

$$\Delta w(\theta) \equiv \mathrm{Cov}(\theta, \theta)^{1/2}, \qquad (30)$$

from Eq. (14) using either $C_{\ell,\mathrm{Exact}}$ (solid blue) or $C_{\ell,\mathrm{Limber}}$ (solid red). The agreement between the theory and mocks is remarkably good for all the range in θ of interest for large scale structure studies, in particular BAO, and all bin configurations. As we move to higher redshifts / wider bins the statistics becomes slightly poorer, but the agreement is still evident. In turn, the Limber approximation overestimates the error by as much 30% for thin bins but it rapidly converges to the exact result for bins wider than $\sim 200\,h^{-1}$ Mpc (e.g. the cases $\bar{z} = 0.3 - \Delta z/(1+z) = 0.15$ or $\bar{z} = 0.5 - \Delta z/(1+z) = 0.15$, at the bottom left panels).

We next discuss the prediction of errors including photo-z effects and redshift space distortions.

The top panel of Fig. 7 shows the r.m.s error in the 125 mocks that incorporate photometric redshift uncertainties as described in Sec. 2.1. The mean redshift was $\bar{z} = 0.5$ and the photo-z error assumed was $\sigma_z = 0.06$ (Gaussianly distributed). The true redshift distribution of objects used in modeling of C_ℓ, Eq. (19), is given in Fig. 4.

We considered two characteristic bin widths, one comparable to the photo-z ($\Delta = 0.075$), and one almost 4 times larger ($\Delta = 0.225$). In both cases the prediction in Eqs. (19-20), shown by solid blue and dashed red lines, is is very good agreement with the mock measurements (in empty and filled symbols).

The bottom panel of Fig. 7 shows instead the r.m.s error obtained from the same bins in redshift space. The prediction, in Eqs. (19-20-21), works to high accuracy in this case as well, for both wide and thin redshift widths. Notice that in the cases shown in this section the error is "sampling variance" dominated (i.e. negligible shot-noise), and therefore is expected to scale with the signal itself. This is reflected in Figs. 6 and 7 where in photo-z space the r.m.s error is smaller than in real space, and viceversa for redshift space.

6.2   Comparing the $w(\theta)$ reduced covariance

Once the diagonal error is well modeled we can turn to the prediction of the full (reduced) covariance matrix. For concreteness we only considered the case of dark-matter and halo mocks in configuration space, i.e. neither photo-z or redshift distortions effects. We fundament this decision in that for a "sampling variance" dominated error, one expects the error to scale roughly with the signal. And we have already shown that we are able to model the signal *and* the variance in all realistic scenarios. The case of "shot-noise" dominated
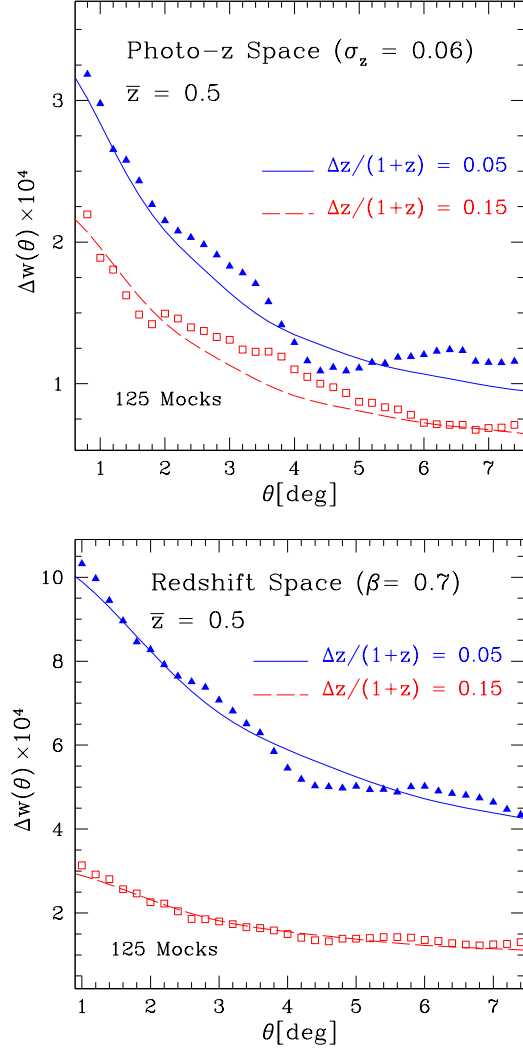

Figure 7. *Errors for $w(\theta)$ in photo-z and redshift spaces*. Top panel shows the r.m.s error in measurements of the angular correlation function in two redshift bins in photo-z space, centered at $\bar{z} = 0.5$, with empty and filled squares respectively (assuming a photo-z of $\sigma_z = 0.06$). The corresponding analytic prediction is given by the solid and dashed lines. Bottom panel shows the comparison of r.m.s errors in mock measurements to the analytical model when redshift space distortions are included (but no photo-z).

error is discussed in detail in Sec. 6.3 and is complementary to redshift distortions or photo-z.

Figure 8 shows the reduced covariance matrix, defined as $\mathrm{Cov}_{\mathrm{Reduced}}(\theta, \theta') = \mathrm{Cov}(\theta, \theta')/\Delta w(\theta)\Delta w(\theta')$, measured from the 324 mocks (left panel) at $\bar{z} = 0.5 - \Delta z/(1+z) = 0.05$ or computed from the expression in Eq. (18) (right panel). They look remarkably similar.

However, a closer look reveals that for a full accord of theory and simulations one needs to include the mode-coupling spectrum (or the one-halo term in the language of the halo-model) and restore some of the high-ℓ tail sup-
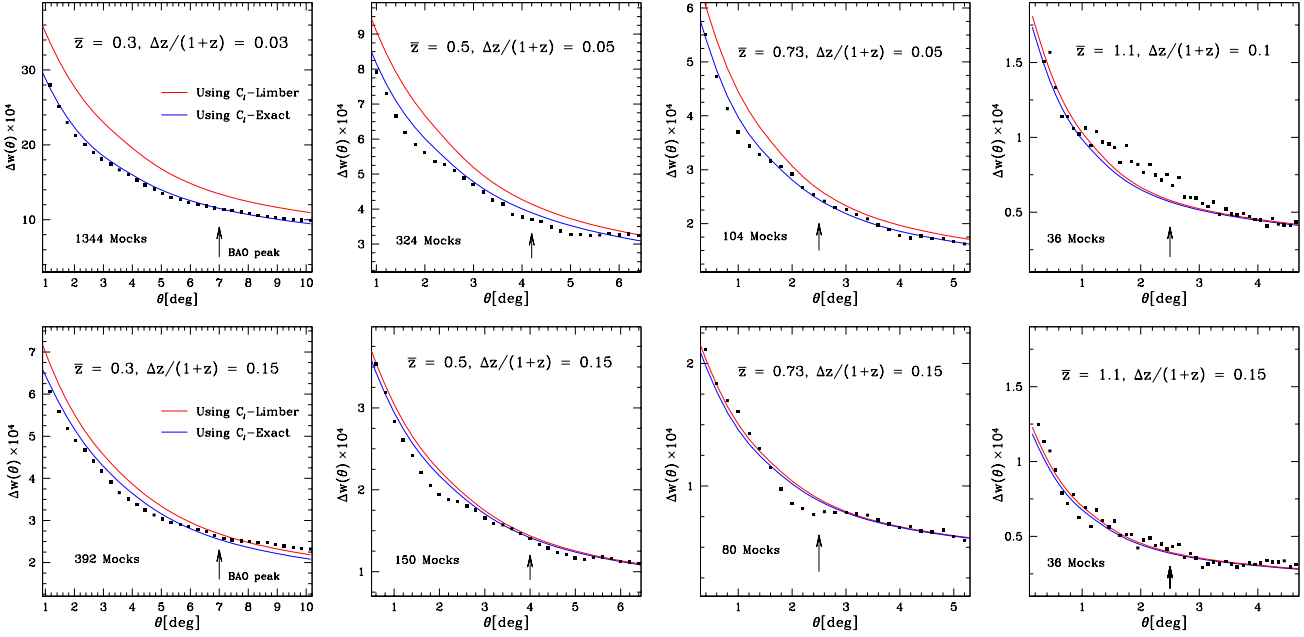
Figure 6. *Error the in Angular Correlation Function.* Predictions for $\Delta w(\theta) \equiv \mathrm{Cov}(\theta,\theta)^{1/2}$ from Eq. (18) using either the exact integration for C_ℓ (blue solid line) or the Limber approximation (red solid line). Symbols are the r.m.s dispersion in measurements of $w(\theta)$ in our ensembles of mock redshift bins. Top panels show thin bins and bottom their wide counter-case. Notice that even as many as 100 mocks can still show sample variance fluctuations in the determination of the error.

pressed by the BAO exponential damping (see Fig. B1). In order to maintain the gains in numerical evaluation of the exact C_ℓ, we do this as follows. We write the linear spatial power spectrum as,

$$P(k) = P_{\mathrm{Lin}}\exp(-k^2 s_{bao}^2) + P_{\mathrm{Lin}}(1 - \exp(-k^2 s_{bao}^2)), \quad (31)$$

and now proceed to evaluate the C_ℓ spectra in two pieces. The low-ℓ contribution using the first term in Eq. (31) with the exact evaluation in Eq. (19) (thus, it does not differ from our proceeding so far). The high-ℓ contribution is obtained inserting the second term in Eq. (31) into the Limber formula, Eq. (B4). In all, we have

$$C_\ell = C_{\ell,\mathrm{Exact}}(P_{\mathrm{Lin}} \times G) + C_{\ell,\mathrm{Limber}}(P_{\mathrm{Lin}} \times (1 - G)) \quad (32)$$

with $G = \exp(-k^2 s_{bao}^2)$. The second term in Eq. (32) has a negligible impact in the estimate of $\Delta w(\theta)$ and will also have in the covariance in cases where the shot-noise of the galaxy sample is not negligible (see Sec. 6.3).

To deepen into the testing of our analytical expressions we plot in Fig. 9 three rows of the reduced covariance matrix, that is, the correlation between $w(\theta)$ and $w(\theta')$ as a function of θ' (at fixed values of θ, as labeled in the plot). We have chosen to do this at our four mean redshits, $z = 0.3, 0.5, 0.73, 1.1$ and characteristics widths $0.15, 0.1, 0.1, 0.15$ respectively (from top to bottom). This election reflects the fact that the calibration of photometric redshifts (mimicked here by the bin width) are better at intermediate redshift, and worse towards low and high z. Solid lines in Fig. 9 are the predictions from Eq. (18) using C_ℓ from Eq. (32). This figure reflects the high degree of correlation between θ-bins even when widely separated,
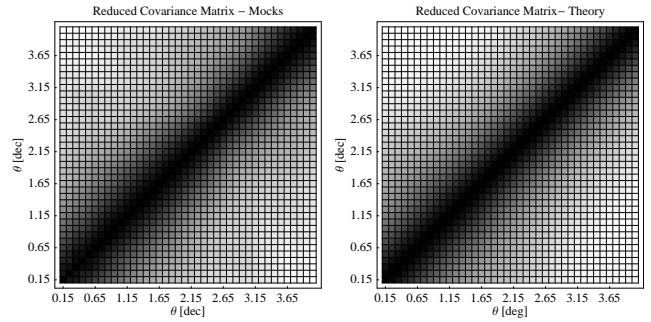

Figure 8. *Reduced Covariance Matrix* for the bin centered at $\bar{z} = 0.5$ and width $\Delta z/(1+z) = 0.05$. *Left panel* shows the measurement over 324 mock red-shift bins (see text) while *Right Panel* shows the prediction for this matrix from Eq. (18).

which is characteristics of Configuration space. Nonetheless the theoretical estimates accounts for the whole shape, particularly close to the diagonal. In all cases, the right-most angle corresponds approximately the angular position of the BAO peak. In turn, Fig. 10 shows the off-diagonal elements of the error matrix $\mathrm{Cov}(\theta, \theta + \Delta\theta)$. Again, the predictions perform very well.

We finish this section comparing theory and mocks at the level of the Singular Value Decomposition, that is many times the only available path to analyze observational data in cases where the covariance matrix is not robustly determined. The top panel of Fig. 11 shows the Singular values for the ensemble of 392 mock-bins with $\bar{z} = 0.5 - \Delta z/(1+z) =$
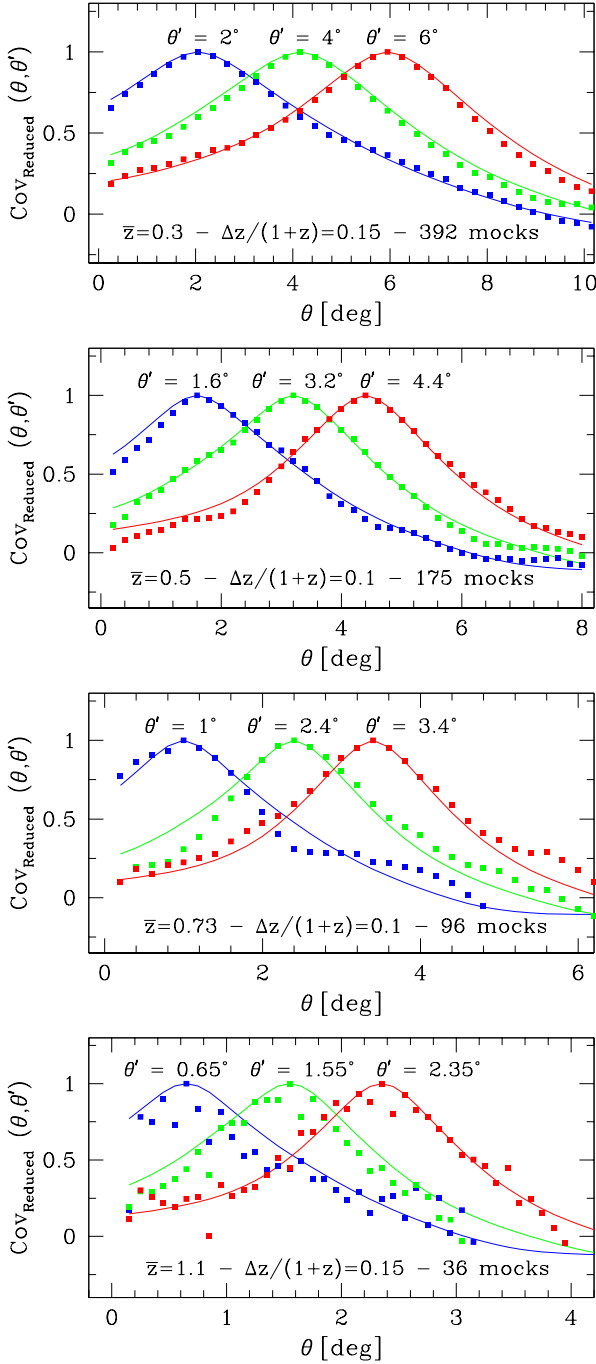
Figure 9. *Rows of the Reduced Covariance Matrix.* Reduced covariance between $\hat{w}(\theta)$ and $\hat{w}(\theta')$ for a fixed value of θ' and as a function of θ. From top to bottom we show bin configurations with larger width at low and high redshifts and smaller at intermediate values (resembling the characteristic performance of photo-z estimates). Solid lines are the predictions from Eq. (18). Notice that close to 200 mocks are necessary for a robust estimation of the covariance. The right-most angle corresponds to the angular BAO scale
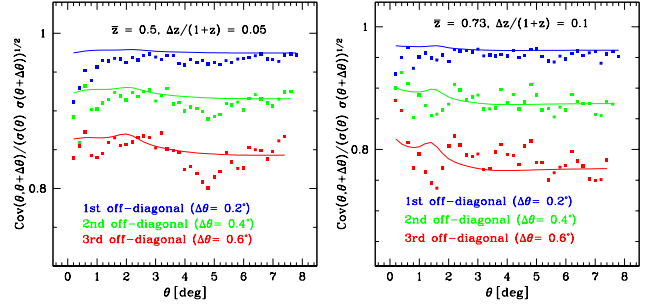
Figure 10. *Off-diagonal Reduced Covariance Matrix.* Reduced covariance between $w(\theta)$ and $w(\theta + \Delta\theta)$ for a fixed value of $\Delta\theta$ and as a function of θ. Mean red-shift and width of each bin configuration are labeled in the plot. Dots correspond to measurements in the 324 or 96 mocks respectively. Solid lines are the predictions from Eq. (18).

0.15. The analytical model, using the linear power spectrum (solid blue line), describe accurately 10 to 15 singular values. We have tested that using more than 10 or 15 singular values the estimate of cosmological parameters have negligible impact in the outcome (see also (Eisenstein & Zaldarriaga 2001)), as they describe very short-range correlations (see bottom panel). These results will be presented in a forthcoming paper (Cabré et al. 2010). There is however, a simple way to improve on the agreement. In dashed line we show the results when using the "measured" C_ℓ spectra in Eq. (18). This indicates that the recovery of these high singular values is affected by the high ℓ tail of C_ℓ where nonlinear effects increase the power over their linear value. On the one hand this will have little importance in practical situations where this regime will be most probably dominated by shot-noise. On the other hand it can be easily modeled using fits to the nonlinear power spectrum, such as `halofit`, into the Limber formula. In the bottom panel of Fig. 11 we show the singular vectors corresponding to singular values 1, 3 and 6.

So far we have not tested our model against measurements of $w(\theta)$ covariance between different redshift bins. However the full covariance matrix in this case can be easily obtained with exactly the same formalism as described in Sec. 3, but using the C_ℓ spectra between the different redshift bins. This is obtained by simply replacing $\Psi_\ell^2 \rightarrow \Psi_{i,\ell}\Psi_{j,\ell}$ in Eq. (19), where Ψ_i is given by Eq. (20) with the radial selection corresponding to the i z-bin.

6.3   The impact of shot-noise

Previous sections showed that the expression in Eq. (18) can describe remarkably well the error due to *sampling variance* in the measurement of the angular correlation function in redshift bins.

We now turn into the problem of describing the error due to shot-noise. To this end we will concentrate on different halo samples as tracers (from Sec. 5.2) and test whether the standard Poisson shot-noise term in Eq. (18) can account for the increase in errors due to their low number density.
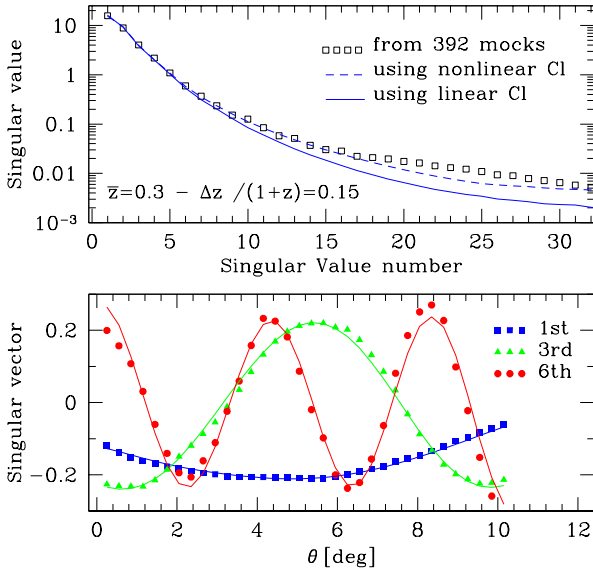
Figure 11. *Singular Value Decomposition* of the Error Matrix measured in 392 mocks at $z = 0.5 - \Delta z/(1+z) = 0.15$. Using the linear power spectrum is possible to reproduce very accurately $\sim$ 15 singular values (top panel) and their singular vectors (bottom panel). Including nonlinear clustering effects into C_ℓ leads to a good match for all singular values. The case shown corresponds to unbiased tracers and negligible shot-noise.

For concreteness we focus on two characteristic z-bin configurations. Figure 12 corresponds to halos with $M \geq 10^{13}\, h^{-1}\, M_\odot$ in the bin at $\bar{z} = 0.3$ and width $\Delta z/(1+z) = 0.15$. This sample has a bias $b(z = 0.3) = 2.36$ (see Fig. 3), what corresponds to $b \sim 2$ if linearly evolved to $z = 0$ (Fry 1996). The sample has an angular abundance of $N/\Omega \sim 17$ halos/deg^2 what gives a shot-noise contribution, Ω/N, of order 2×10^{-7}sr^2. This corresponds to $\bar{n}\, b^2\, C_\ell \sim 1$ at $\ell \sim 200$.

Top panel of Fig. 12 shows the r.m.s. error measured in the ensemble of 392 mock redshift bins while lines are the predictions from Eq. (18) using the exact C_ℓ integration and including Poisson shot-noise (solid blue) or neglecting it (dashed blue). As we see the presence of shot-noise increases the error by 20% (in this case), but this can be very well modeled by the addition of the simple Poisson shot-noise $1/\bar{n}$ contribution to C_ℓ. Bottom panel shows the singular values of the covariance matrix SVD. Almost none of the singular values is well recovered when shot-noise is neglected.

In turn, Fig. 13 corresponds to halos with $M \geq 2 \times 10^{13}\, h^{-1}\, M_\odot$ at higher redshift, in the bin $\bar{z} = 0.5 - \Delta z/(1 + z) = 0.1$ (the halo mass-cut was chosen slightly higher at higher redshift to resemble a flux-limited survey). In this case the bias is $b(z = 0.5) = 2.93$ ($b \sim 2.3$ at $z = 0$) with an angular abundance of $N/\Omega \sim 11$ halos/deg^2 ($\bar{n}\, b^2\, C_\ell \sim 1$ at $\ell \sim 200$). The shot-noise increases the error by $\sim 30\%$ on top of the sampling variance (solid vs. dashed lines in the top panel) and plays a crucial role in the SVD eigenvalues (bottom panel).
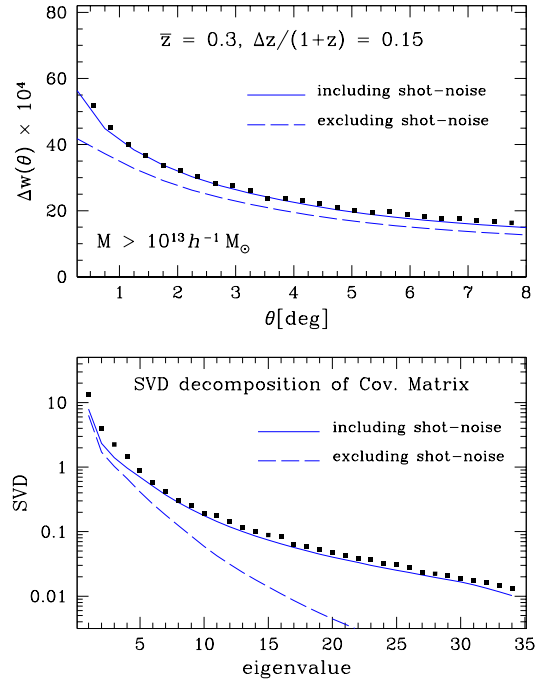

Figure 12. *The effect of shot-noise at $z = 0.3$.* Diagonal error (top panel) and Singular Value Decomposition of the Covariance Matrix (bottom panel) for the bin $z = 0.3$ and $\Delta z/(1+z) = 0.15$ for a sample of halos with $M > \times 10^{13}\, h^{-1}\, M_\odot$. The (Poisson) shot-noise term increases the error by $\sim 20\%$ on top of sampling variance (solid and dashed lines are the model with and without the $1/\bar{n}$ term) and is critical to recover the correct singular eigenvalues. We used 392 mocks for this case.

Remarkably, in both cases (Figs. 12 and 13), the inclusion of the simple Poisson white-noise on top of the sampling variance in Eq. (18) accounts very well for all singular values as well as the diagonal error (solid lines).

Arguably, the halo samples used in this test are too much dominated by shot-noise. We have also done the exercise of gradually increasing the relative contribution of shot-noise in front of sampling variance by increasingly under-sampling the dark matter field. As expected, the error is always recovered by the model just by increasing the Poisson term in Eq. (18) accordingly.

7 CONCLUSIONS

The field of large scale cosmological structure will undergo an unprecedented era in the immediate future with several large observational campaigns proposed or under implementation. Many of these surveys, such as DES, PanStarrs and LSST, will use photometric techniques to estimate the radial position of galaxies instead of measuring their full spectra, which is more time-demanding . This gain allows to survey wider areas and fainter objects, but at the exchange of increasing the uncertainties in the true redshifts and degrading the radial clustering amplitude. The proposal is then to
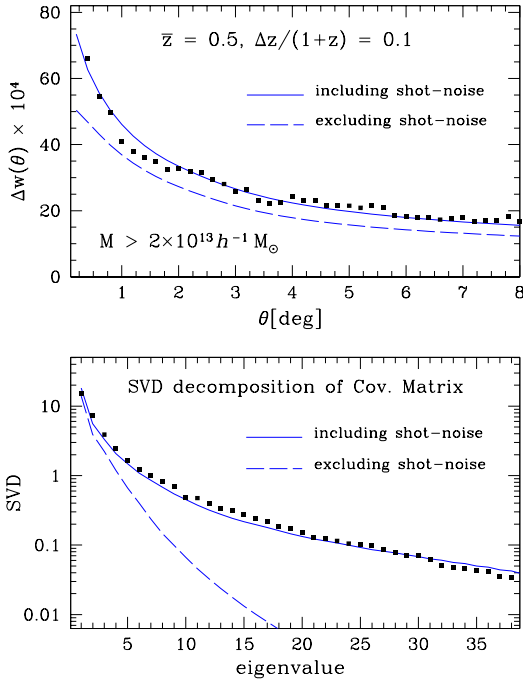
Figure 13. *The effect of shot-noise at $z = 0.5$. Diagonal error (top panel) and Singular Value Decomposition of the Covariance Matrix (bottom panel) for the bin $z = 0.5$ and $\Delta z/(1+z) = 0.1$ for halos with $M > 2 \times 10^{13}\, h^{-1}\, \mathrm{M}_\odot$. Conclusions shared with Fig. 12. We used 175 mocks for this test.*

split the data into redshift bins and exploit the information available from angular correlation functions, provided with an accurate determination of the measurement errors. Yet, this goal can only be accomplished if we develop accurate models for the signal and its errors that take into account all relevant effects and are robustly tested in realistic scenarios. In this paper we addressed this issue in a comprehensive way.

We first developed an extensive set of mock catalogues (in the form of redshift bins) reproducing the angular coverage, photo-z and radial distribution of a photometric survey like DES. For this we used a large N-body simulation (of $\sim 450\, h^{-3}\, \mathrm{Gpc}^3$ simulated volume) provided by the MICE collaboration (http://www.ice.cat/mice). These mocks can be regarded as independent realizations as their volume overlap is minimal and therefore provide a unique statistical framework for model testing (see Table 1). They are also equivalent to a light-cone analysis as we are doing redshift bins.

We next developed a model for the angular correlation function $w(\theta)$ accounting for all the relevant effects, namely bin projection, nonlinear gravitational evolution, linear bias, redshift space distortions and photo-z errors.

An exhaustive comparison of our model for $w(\theta)$ against the mock measurements showed a remarkably good agreement for a wide range of θ, validating the treatment of the different effects and opening the door of the use of this probe for real data analysis. Nonlinear gravitational evolution pro-

duces minor distortions in the correlation pattern after the bin projection. In turn, analysis of halo angular clustering showed a very good consistency with a linear bias assumption. The interplay of photo-z and redshift distortions is the most important consideration regarding the shape of $w(\theta)$.

Redshift space distortions introduces a large and scale dependent enhancement of $w(\theta)$, that can reach a factor of a few at BAO scales (see Fig. 5). For our widest bin (where the effect should be least important) it still rises the amplitude of $w(\theta)$ by $\sim 50\%$ at θ_{BAO} (with respect to the true redshifts case). Conversely, photo-z effects lower the clustering amplitude by extending the effective bin projection. For example, for the widest bin mentioned before we find that the two effects counter-act each other at θ_{BAO}, but leave a scale dependent signal towards smaller angles.

In turn, we showed that the Limber approximation should not be used in precision analysis of large scale clustering as it leads to the incorrect shape of $w(\theta)$ in the full range of interesting scales, and severely misestimates the amplitude of the C_ℓ spectra for $\ell \lesssim 40-50$. This is convincingly shown in Figs. B1, B2 and B3.

We would like to highlight that, in the process of describing $w(\theta)$, we have also investigated a model for the 3-d matter correlation function that is able to reproduce the clustering signal in a broad range of scales and redshifts with only 2 parameters. This, discussed in detail in Appendix A, can be of grand interest for future spectroscopic surveys such as BOSS, Hetdex and WiggleZ.

We have made an equally exhaustive effort in modeling and testing the full error matrix characterizing the measurements of $w(\theta)$. The covariance matrix is often estimated from the data itself, using internal or re-sampling methods such as Jack-knife or bootstraping. However, their limitation is still a matter of some debate (Norberg et al. 2009). Having a full theoretical model is thus very suitable for present and future analysis.

We took into account partial sky coverage by assuming that $\mathrm{Cov}(\theta, \theta')$ scales as f_{sky}^{-1}. The full sky situation is then easily treated by translating errors from harmonic space, where the covariance matrix is diagonal and proportional to C_ℓ. Through the angular power spectra we included the same effects considered for $w(\theta)$ into $\mathrm{Cov}(\theta, \theta')$ (photo-z, redshift distortions, bias) for a typical survey with $f_{sky} = 1/8$.

Our modeling of errors recovers the correct variance in $w(\theta)$ as measured in the mocks for a wide range of bin configurations, from low to high redshift ($z \sim 0.3-1.1$) and from thin to thick bins ($100\, h^{-1}\, \mathrm{Mpc} - 550\, h^{-1}\, \mathrm{Mpc}$). And this conclusion extend to the more realistic cases where we included photo-z effects and redshift space distortions. In addition we used different halo samples to study cases where the shot-noise was comparable or larger than the sample variance component of the error. This regime was also nicely described analytically by adding a standard Poisson shot-noise contribution to the variance of the C_ℓ spectra.

Moreover, and thanks to the large number of mocks constructed, we measured the full covariance matrix with high precision in different configurations. We find that at least $150-200$ mocks are necessary for a well defined reduced covariance, but this is discussed more properly in Cabré et

al. 2010. Remarkably in all cases tested, the modeling recovers very accurately the true error matrix.

In a parallel line of research we have tested the recovery of cosmological parameters using our model for $w(\theta)$ and the theoretical expression of the covariance matrix. And compared this with the same analysis but using the *true covariance* as measured in the mock ensembles. Indeed, the best-fit values and errors contours coincide for both approaches (Cabré et al. 2010) giving very encouraging prospects for the use of our analytical expressions in real data analysis or in realistic forecasts of upcoming photometric surveys.

The code implementing the models presented in this paper will be publicly available at `sites.google.com/site/martincrocce/public-codes`

ACKNOWLEDGMENTS

REFERENCES

Banerji, M., Abdalla, F. B., Lahav, O., Lin, H., MNRAS, **386** 1219 (2008)
Bernstein, G., ApJ, **424**, 569 (1994)
Bernstein, G., Huterer, D., MNRAS, **401**, 1399 (2010)
Blake, C., Collister A., Bridle S., Lahav, O., MNRAS, **374**, 1527 (2007)
Budavári, T., et al., ApJ, **595**, 59 (2003)
Cabré, A., Fosalba, P., Gaztañaga, E., Manera, M., MNRAS, **381**, 1347 (2007)
Cabré, A., Crocce, M., Gaztanãga, E., *in prep*, (2010)
Cai, Y-C, Angulo, R. E., Baugh, C. M.; Cole, S., Frenk, C. S., Jenkins, A., MNRAS, **395**, 1185 (2009)
Cole, S., et al., MNRAS, **362**, 505 (2005)
Colless M., et al., e-print arXiv:astro-ph/0306581 (2003)
Crocce, M., Fosalba, P., Castander, F. J., Gaztañaga, E., MNRAS, **403**, 1353 (2010)
Crocce, M. and Scoccimarro, R., PRD, **73**, 063519 (2006a)
Crocce, M. and Scoccimarro, R., PRD, **73**, 063520 (2006b)
Crocce, M. and Scoccimarro, R., PRD, **77**, 023533 (2008)
Desjacques, V., Sheth, R. K., PRD, **81**, 023526 (2010)
Dodelson S., *Modern Cosmology*, p. 342 Eq. 11.27, Academic Press Inc., U.S. (2003)
Eisenstein, D. J., Zaldarriaga, M., MNRAS, ApJ, **546**, 2 (2001)
Eisenstein, D. J., et al., M., ApJ, **633**, 560 (2005)
Eisenstein, D. J., Seo, H-J., White, M., ApJ, **664**, 660 (2007)

Evrard A. E., et al., ApJ, **573**, 7, (2002)
Fisher, K. B., Scharf, C. A., Lahav, O., MNRAS, **266**, 219 (1994)
Fosalba, P., Gaztañaga, E., Castander, F. J., Manera, M., MNRAS, **391**, 435 (2008)
Fry, J. N., ApJ, **461**, L65+, (1996)
Gaztañaga, E., Cabré, A., Hui, L., MNRAS, **399**, 1663 (2009)
Górski, K. M., Hivon, E., Wandelt, B. D., in Proc. MPA- ESO Conf., Evolution of Large-Scale Structure: From Re- combination to Garching, p.37, (1999). Ed. A.J.Banday, R.K.Seth, and L.A.N. da Costa (Enschede: PrintPartners Ipskamp)
Hearin, A. P., Zentner, A. R., Ma, Z., Huterer, D., ApJ *submitted*, e-print arXiv:astro-ph/1002.3383
Hamilton, A. J. S., ApJ, **385**, L5 (1992)
Kaiser, N., MNRAS, **227**, 1 (1987)
Kaiser, N., ApJ, **388**, 272 (1992)
Kaiser, N., ApJ, **498**, 26 (1998)
Komatsu, E., et al., e-print arXiv:astro-ph/1010.4538 (2010)
Limber, D. N., ApJ, **117**, 134 (1953)
LoVerde, M., Afshordi, N., PRD, **78** 123506 (2008)
Ma, Z., Hu, W., Huterer D., ApJ, **636**, 21 (2006)
Manera, M., Gazatanãga, E., e-print arXiv:astro-ph/0912.0446 (2009)
Matarrese, S., Pietroni, M., Modern Phys. Letters A., **23**, 25 (2008)
Matsubara, T., ApJ, **615**, 573 (2004)
Matsubara, T., PRD, **77**, 06330 (2008)
Meneux, B. et al., A&A, **505**, 463 (2009)
McDonald, P., Trac, H., Contaldi, C., MNRAS, **336**, 547 (2006)
Nock, K., Percival, W. J., Ross, A. J., MNRAS *submitted*, e-print arXiv:astro-ph/1003.0896
Norberg, P., Baugh, C. M., Gaztañaga, E., Croton, D. J., MNRAS, **396**, 19 (2009)
Padmanabhan, N. et al., MNRAS, **359**, 237 (2005)
Padmanabhan, N. et al., MNRAS, **378**, 852 (2007)
Peebles, P. J. E., ApJ, **185**, 413 (1973)
Percival, W. J., et al., MNRAS, **401**, 2148 (2010)
Perlmutter, S., et al., ApJ, **517**, 565 (1999)
Reid, B., et al., MNRAS, **404**, 60 (2010)
Riess, A.G., et al., ApJ, **116**, 1009 (1998)
Ross, N. P. et al, MNRAS, **381**, 573 (2007)
Sánchez, A. G., Baugh, C. M., Angulo, R., MNRAS, **390**, 1470 (2008)
Sánchez, A. G., Crocce, M., Cabré, A., Baugh, C. M., Gaztañaga, E., MNRAS, **400**, 1643 (2009)
Sawangwit, U., Shanks, T., Abdalla, F. B., Cannon, R. D., Croom, S. M., Edge, A. C., Ross, Nicholas P., Wake, D. A., e-print arXiv:astro-ph/0912.0511 (2009)
Seo, H-J., Eisenstein, D. J., ApJ, **633**, 575 (2005)
Simon, P., A&A, **473**, 711 (2007)
Simpson, F., Peacock, J. A., Simon, P., PRD, **79**, 063508 (2009)
Smith, R., Scoccimarro, R., Sheth, R. K., PRD, **77**, 043525 (2008)
Springel, V., MNRAS, **364**, 1105 (2005)
Taruya, A., Nishimichi, T., Saito, S., Hiramatsu, T., PRD, **80**, 123503 (2009)
York D.G., et al., ApJ, **120**, 1579 (2000)

APPENDIX A: SPATIAL CLUSTERING

In Sec. 2.2 we presented a parametric model for the spatial correlation function and argued that a single set of best-fit parameters could be used to describe the clustering from low to high redshift. In this appendix we show how this model

performs against measurements of 3-d clustering in N-body simulations, in particular *as a function of redshift.*

A0.1   Nonlinear Gravitational Clustering

The top panel of Fig. A1 shows the spatial correlation function measured in MICE7680 at $z = 0.3$ compared with the parametric model given in Eq. (10) for best-fit parameters $s_{bao} = 5.54 \, h^{-1}$ Mpc and $A_{mc} = 1.55$. To simplify the measurement we only used a cubic sub-volume of the full comoving output, of length $L_{\rm box} = 2560 \, h^{-1}$ Mpc. Error bars were obtained from the scatter among 125 Jack-knife volumes of the full box. We see that the model performs very well down to scales $\sim 20 \, h^{-1}$ Mpc at this redshift. Notice how the convolution of linear theory with a Gaussian smoothing (dot dashed line) leads to a slight increase in amplitude above the measurements for $r \lesssim 60 \, h^{-1}$ Mpc. Measurements follow linear theory at these scales. The effect of the mode-coupling term in Eqs. (8,10) is mainly to correct for this mismatch.

From theoretical grounds we expect the smoothing length to be determined by the amplitude of large-scale velocity flows and therefore given by ((Crocce and Scoccimarro 2006b; Matsubara 2008),

$$s_{bao} \sim [(1/3) \int d^3 q P_{\rm Lin}(q)/q^2]^{1/2} = 5.42 \, {\rm Mpc} \, h^{-1} \quad (A1)$$

which is within 3% agreement with the recovered best-fit value. In turn, the lowest order estimation for A_{mc} using perturbation theory yields $34/21 \sim 1.62$ independently of cosmology and redshift (Crocce and Scoccimarro 2008), which is also very close to our best-fit value 1.55.

Hence, it is possible to use these theoretical estimates as a starting point in the modeling instead of using fitting parameters. Notice however that, if one extrapolates this model to describe the clustering of tracers, the actual values for s_{bao} and A_{mc} might depend on the particular tracer under study (e.g. on halo mass) (Sánchez et al. 2008). In addition, the rather large error bars obtained from present day data do not put severe constraints on the values of s_{bao} and A_{mc} (Sánchez et al. 2009; Percival et al. 2010).

The standard approach for analyzing clustering data in a photometric redshift survey covering from low ($z \sim 0.2$) to high redshift ($z \sim 1.4$) is to divide the data into several redshift bins (whose minimum width are ultimately determined by the photo-z accuracy). If one then performs a joint analysis of all these bins it is desirable to have the least number of nuisance parameters possible in order to optimize constraints on derived cosmological parameters. With this approach in mind we now show to what extent a single set of best-fit parameters can be used to describe the 3-d clustering from low to high redshift, and hence the angular clustering after the projection in Eq. (5).

The bottom panel of Fig. A1 shows our model in Eq. (10) against measurements of ξ in the comoving outputs of MICE7680 at $z = 0.5$, 0.73 and 1.1. The values for s_{bao} and A_{mc} were taken from a best-fit analysis to $\xi(r)$ at $z = 0.3$. In all cases the agreement is very good, similar to that at $z = 0.3$.

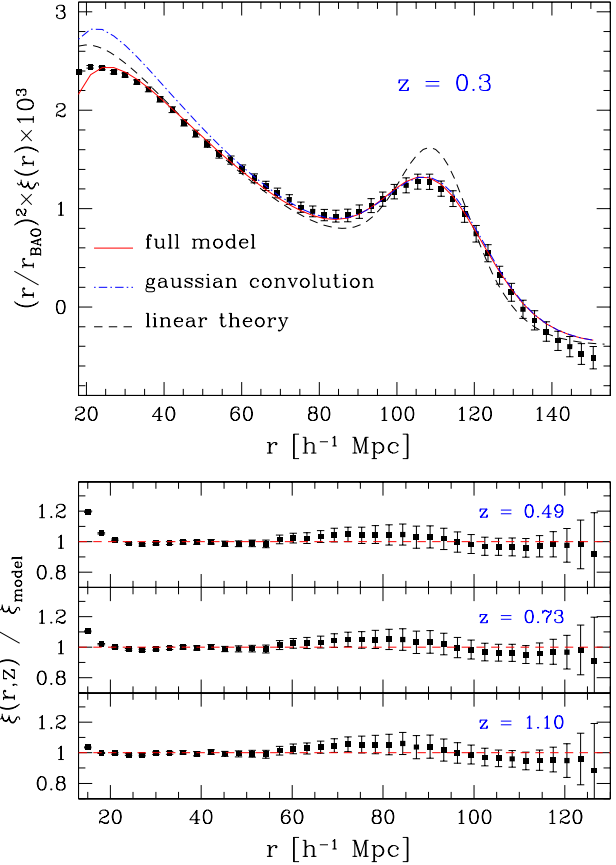Notice that conclusion in this appendix relate to 3-d

Figure A1. *Spatial Correlation Function:* measured in the $z = 0.3$ comoving output of a large volume N-body run (MICE7680) compared with the parametric model given in Eq. (8) with best-fit parameters $s_{bao} = 5.54 \, h^{-1}$ Mpc and $A_{mc} = 1.55$ (Top panel). The length scale used in the y-axis is $r_{BAO} = 110 \, h^{-1}$ Mpc. Bottom panels display the ratio of the measured correlation function (at the given redshift) to our model correlation, obtained after scaling with redshift the $z = 0.3$ best-fit values.

clustering in general, regardless of photo-z, hence are also relevant for spectroscopic surveys such as BOSS [12], Hetdex [13] and WiggleZ [14].

APPENDIX B: THE LIMBER APPROXIMATION

B1 C_ℓ power spectrum : exact evaluation and Limber formula

In this appendix we discuss the way we implement the numerical integrations that lead to the exact C_ℓ spectra in Eqs. (19,20), and how this exact results compare with the widely used Limber approximation (Limber 1953).

[12] http://www.sdss3.org/
[13] http://hetdex.org/
[14] http://wigglez.swin.edu.au/

Let us first recall the derivation of the exact expression of the angular power spectrum in terms of the spatial one. This is done by expanding the density field in Eq. (1) in Fourier Series and subsequently expanding the plane wave into spherical harmonics [15]. After some straightforward manipulation this leads to,

$$a_{\ell m} = 4\pi i^{\ell} \int dz\, \phi(z) \int \frac{d^3 k}{(2\pi)^3} \delta(\mathbf{k}, z) j_{\ell}(k\, r(z)) Y^{\star}_{\ell m}(\hat{\mathbf{k}}),$$
(B1)

where j_{ℓ} are the spherical Bessel functions of order ℓ. Inserting Eq. (B1) into Eq. (13) gives Eqs. (19,20),

$$C_{\ell,\mathrm{Exact}} = \frac{1}{2\pi^2} \int 4\pi k^2 dk P(k) \Psi_{\ell}^2(k)$$

$$\Psi_{\ell}(k) = \int dz \phi(z) D(z) j_{\ell}(kr(z))$$

These integral expressions are numerically expensive to compute due to the oscillatory behavior of the spherical Bessel functions $j_l(x)$ for $x \gg 1$. It is then desirable to seek for ways to improve their convergence.

Since we are interested in large scales we proceeded as follows. The degradation of the BAO bump due to non-linear effects can be modeled to a large extent by simply introducing an exponential damping to the large-scale power spectrum, i.e.

$$P_{\mathrm{NonLin}}(k, z) = P_{\mathrm{Lin}}(k, z) \exp(-k^2 \sigma_v^2 D^2(z))$$
(B2)

with $\sigma_v \approx 7\, \mathrm{Mpc}\, h^{-1}$, depending on cosmology (this is the parameter we called s_{bao} in Sec. 2.2). This natural cut-off in Fourier space leads to the correct shape of the 3-d correlation function in a broad range of scales, e.g. Fig A1. In the same way, one can then speed-up the evaluation of the exact integrals in Eqs. (19,20) by adopting an exponentially suppressed spectrum and integrate only up to an upper bound $k_{\max} \sigma_v \sim 4 - 5$, since our goal is the description of large-scale angular correlation function. In what follows we will always adopt this approach to evaluate $C_{\ell,Exact}$.

In turn, the most popular short-cut to evaluate Eqs. (19,20) is the so-called Limber approximation (Limber 1953; Kaiser 1992; Kaiser 1998) that follows from the orthogonality relation of the spherical Bessel functions (e.g. see Loverde and Afshordi 2008),

$$\int dk k^2 j_l(kr_1) j_l(kr_2) P(k)$$
(B3)

$$\approx \frac{\pi}{2} \frac{\delta^{\mathrm{D}}(r_1 - r_2)}{r_1^2} P(k = \frac{l + 1/2}{r}),$$

that leads to the well-known expression,

$$C_{\ell,\mathrm{Limber}} = \int dz \phi^2(z) D^2(z) P((\ell + 1/2)/r(z)) \frac{H(z)}{r(z)^2}.$$
(B4)

Strictly speaking this is valid for $\ell \gg 1$ (that is, small angles) therefore it is appropriate to discuss the limits of applicability of this approximation to very large-scales, as those probed by BAO.

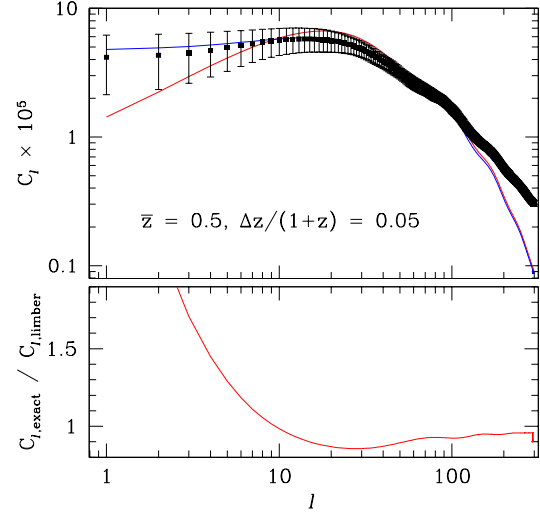In the top panel of Fig. B1 we show the measured C_{ℓ}

Figure B1. *Angular Power Spectrum* measured in the 324 mock catalogues of mean redshift $\bar{z} = 0.5$ and width $\Delta z/(1 + z) = 0.05$ (see Table I), compared with the theoretical prediction from the exact integration in Eq. (19) (solid blue line) and the Limber approximation in Eq. (B4) (solid red). The Limber approximation leads to a severe under-estimation of the large angle power ($l \leq 30$) that critically impact the computation of the angular correlation function at large BAO scales.
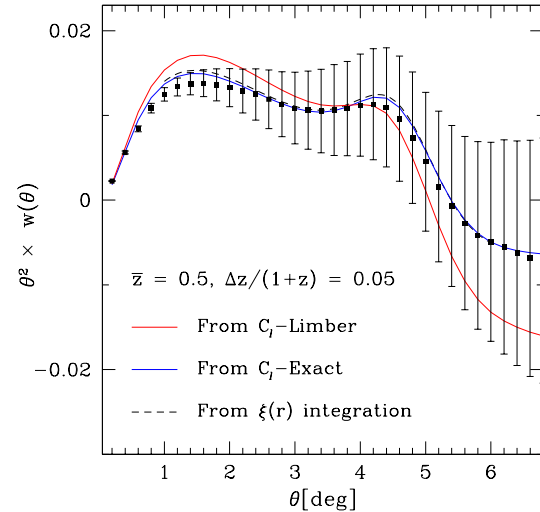

Figure B2. *Angular Correlation Function* measured in the 324 mock bins compared with the theoretical predictions obtained from Eq. (5) (dashed line), or from C_{ℓ}-space through the Legendre polynomials and Eq. (14). Using the Limber approximation to compute the C_{ℓ} leads an incorrect shape for $w(\theta)$ (solid red line). In turn, the exact C_{ℓ} integration agrees as expected with Eq. (5) (solid blue line).

[15] $e^{ikr\hat{\mathbf{k}}\cdot\hat{\mathbf{n}}} = 4\pi \sum_{\ell \geq 0} \sum_{m=-\ell}^{\ell} i^{\ell} j_{\ell}(kr) Y_{\ell m}(\hat{\mathbf{k}}) Y^{\star}_{\ell m}(\hat{\mathbf{n}})$

power spectrum averaged over 324 mocks red-shift bins centered at $\bar{z} = 0.5$ with $\Delta z/(1 + z) = 0.05$. The solid blue line corresponds to the exact integration and the solid red line to the Limber approximation in Eq. B4 (in both cases with $P(k)$ from Eq. B2 and the best-fit value for s_{bao} from Sec. 2.2). Clearly, the Limber approximation fails by a large factor at low-l (see bottom panel). This is in agreement with the recent work by Loverde and Afshordi 2008, who circumvents this short-coming by including 2-*nd* order corrections to the Limber formula. We have not explored this possibility as the numerical evaluation of the exact C_ℓ expression as proposed above is fast enough for our purposes. Yet, notice how by $l \geq 100$ the exponential damping of the linear power spectrum $P(k)$ suppresses the amplitude of harmonic space power. This shows that our approach for a fast evaluation of the spherical Bessel functions is not appropriate for modeling the shape of C_ℓ at weakly non-linear scales where one would need to add the boost of power due to mode-coupling effects (Crocce and Scoccimarro 2008). A simple way to implement this is discussed in more detail in Sec. 6.2, Eqs. (31,32).

B2 Correlation Function : results in Real and Redshift Space

The inaccuracy of the Limber approximation also affects the calculations in configuration space. For instance, the way in which the disagreement in Fig B1 translates into Real Configuration Space is depicted in Fig. B2. Solid red and solid blue lines were obtained using Eq. (14) and C_ℓ from the Limber or the Exact evaluation respectively. Dashed line follows from projecting the 3-d correlation function, as in Eq. (5). Here, the failure of the Limber approximation to describe the BAO bump is even more evident. The exact C_ℓ integration yields almost the same result as the one from Eq. (5), as expected.

These limitations are even more severe when redshift distortions are taken into account. Without lost of generality we will use a top-hat selection in the following equations to illustrate the problem:

$$w(\theta) = \frac{1}{\Delta_\chi^2} \int_{\chi_{min}}^{\chi_{max}} d\chi_1 \int_{\chi_{min}}^{\chi_{max}} d\chi_2 \; \xi(r_1, r_2) \qquad \text{(B5)}$$

where $\Delta_\chi \equiv \chi_{max} - \chi_{min}$. The correlation $\xi(r_1, r_2)$ is only a function of the relative separation between r_1 and r_2. Because of redshift distortions, this is in fact a function of π and σ, the light-of-sight and transverse separation. For small angles and distance observer, i.e. the Limber approximation, we can take $\pi = \chi_2 - \chi_1$ and $\sigma^2 = \chi_1\chi_2\theta^2$ [16]. We can then change variables in the above integrals from χ_1 and χ_2 to π and σ

$$w(\theta) = \frac{2}{\theta \Delta_\chi^2} \int_{\sigma = \chi_{min}\theta}^{\sigma = \chi_{max}\theta} d\sigma \int_{\pi=0}^{\pi=\Delta_\chi} d\pi \; \xi(\pi, \sigma) \qquad \text{(B6)}$$

This result is valid both in real and redshift space. In real space, $\xi(\pi, \sigma)$ is replaced by the isotropic correlation

---

[16] For a non-flat cosmology we need to replace χ by the comoving angular diameter $D(\chi)$ distance here: $\sigma^2 = D(\chi_1)D(\chi_2)\theta^2$

$\xi(r)$ with $r^2 = \pi^2 + \sigma^2$. In redshift space we use the linear theory prediction (Kaiser 1987; Hamilton 1992):

$$\xi(\sigma, \pi) = \xi_0(s)P_0(\mu) + \xi_2(s)P_2(\mu) + \xi_4(s)P_4(\mu) \qquad \text{(B7)}$$

where π and σ represent the separation along and transverse to the line-of-sight (l.o.s) and ξ_ℓ are the multi-poles of the correlation function in terms of Legendre polynomials P_ℓ,

$$\xi_\ell(s) = \frac{2\ell + 1}{2} \int_{-1}^{+1} \xi(\pi, \sigma) P_\ell(\mu) d\mu, \qquad \text{(B8)}$$

with $s = \sqrt{\sigma^2 + \pi^2}$ and μ is the cosine angle with the l.o.s. For the Kaiser model one has (Hamilton 1992),

$$\xi_0(s) = b^2 \left(1 + \frac{2\beta}{3} + \frac{\beta^2}{5}\right) \xi(s) \qquad \text{(B9)}$$

$$\xi_2(s) = b^2 \left(\frac{4\beta}{3} + \frac{4\beta^2}{7}\right) [\xi(s) - \bar{\xi}(s)] \qquad \text{(B10)}$$

$$\xi_4(s) = b^2 \frac{8\beta^2}{35} \left[\xi(s) + \frac{5}{2}\bar{\xi}(s) - \frac{7}{2}\bar{\bar{\xi}}(s)\right] \qquad \text{(B11)}$$

where b is the bias of the sample (assumed linear and local), $\beta = f/b$, $f = \partial \ln D / \partial \ln a$ is the growth rate factor and

$$\bar{\xi}(r) = \frac{3}{r^3} \int_0^r \xi(r')r'^2 dr', \qquad \text{(B12)}$$

$$\bar{\bar{\xi}}(r) = \frac{5}{r^5} \int_0^r \xi(r')r'^4 dr'. \qquad \text{(B13)}$$

We will show next that Eq. (B6) turns out to be a bad approximation to model BAO scales. But it provides a good way to illustrate why redshift space distortions are so important for the BAO detection for small (to moderate) photo-z bin widths Δ_χ. For large values of Δ_χ the integral reproduces the real space correlation (because the total number of pairs are preserved by redshift space distortions), while for $\Delta_\chi < 500\,h^{-1}$ Mpc the π integral is truncated by the radial boundary of the top-hat window. Line-of-sight pairs separated by $\pi > \Delta_\chi$ do not enter in the redshift bin and are therefore not integrated. Smaller pairs are also affected because many of them are missing at the boundaries. This missing pairs produce a distortion in the measured $w(\theta)$ as compared to real space correlation (see Fisher et al. 1994, Padmanabhan et al. 2007 and Nock et al. 2010).

Both real and redshift results are quite inaccurate under the Limber approximations. This is illustrated in Fig. B3, which compares the calculation of the above integral in real and redshift space in the Limber approximation (dashed lines) with the corresponding exact results (continuous line) by integrating Eq. (B5). Note how the results in real space are very similar to the corresponding calculation in Fig. B2, based on power spectrum calculation. The results in redshift space for the Limber approximations show even larger deviations than in real space. The BAO peak, which shows around $\theta \simeq 4°$ is clearly distorted by the Limber approximation. We conclude that the Limber approximation is not good enough for precision BAO modeling and we use the exact integration throughout this paper.
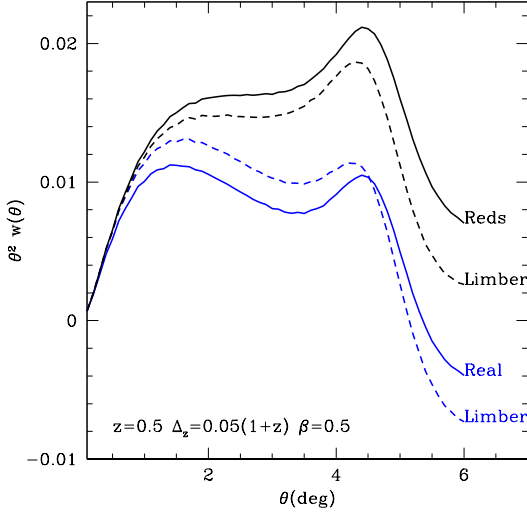
Figure B3. Angular correlation in the Limber approximation (dashed line) in Eq. (B6) in both real (bottom dashed line) and redshift space (top dashed line). Continuous lines show the corresponding exact calculations using Eq. (B5).

APPENDIX C: ERRORS IN HARMONIC SPACE

In this appendix we comment briefly on the correlation between different modes in Harmonic Space induce by a partial sky coverage. We leave a more detailed discussion of this important issue for future work.

Equation (18) can be naively interpreted as if, in the presence of a partial sky coverage, the errors in C_ℓ increase by a factor $1/\sqrt{f_{sky}}$ with the co-variance matrix remaining diagonal, that is

$$(\Delta C_\ell)^2 \approx \frac{1}{f_{sky}} \frac{2}{2\ell+1} C_\ell^2 \qquad (C1)$$

This is not the case in reality, the presence of boundaries does increase the error but it also introduces co-variance between different ℓ modes (e.g. Cabré et al. 2007 and references therein). Figure C1 shows the covariance in Harmonic space between C_ℓ measurements using 392 mocks with $\bar{z} = 0.5$ and $\Delta z/(1+z) = 0.1$. As we can see in the bottom panel the error is not diagonal but distributed in a range of ℓ values approximately given by $\pm 1/f_{sky}$. Remarkably, for a given value of ℓ' the integral,

$$\int d\ell \, \text{Cov}(\ell', \ell) \approx \frac{2}{f_{sky}(2\ell'+1)} C_{\ell'}^2 \qquad (C2)$$

what leads to the simple interpretation that, when the survey is reduced from a full-sky limit by a fraction f_{sky}, the diagonal covariance rises from its value $2/(2l+1)$ by a factor $1/f_{sky}$ and "leaks" towards other ℓ modes resulting in a non-diagonal error matrix. The final diagonal error is smaller that its "full-sky" value (e.g. as shown in the top panel of Fig. C1) but is the off-diagonal elements of $\text{Cov}(\ell, \ell')$ what determine $\text{Cov}(\theta, \theta')$. Yet, we circumvent the problem of computing non-diagonal components of $\text{Cov}(\ell, \ell')$ by assum-
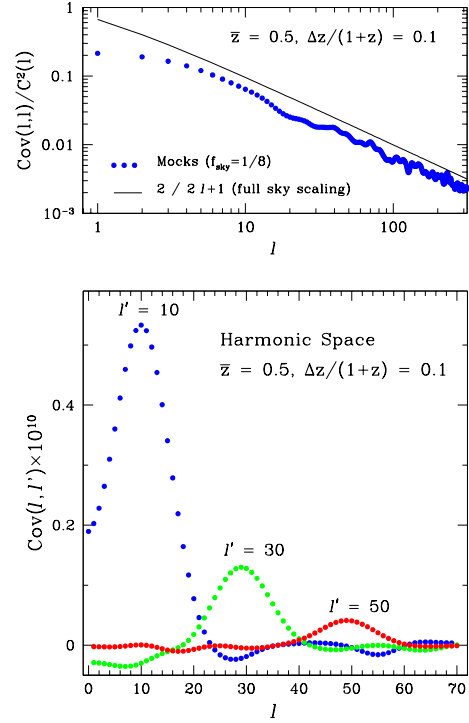

Figure C1. *Correlations of Cl spectra induced by partial sky coverage.* The *total* error budget in a partial sky survey increases (roughly by a factor $1/f_{sky}$) compared to the full sky case. The covariance matrix is no longer diagonal (bottom panel) with the variance error smaller than its full sky value, by 30% in this particular case, as shown in the top panel (see text for details).

ing the scaling of the covariance in Configuration space as $1/f_{sky}$.

A possible way to overcome the complex covariance in Harmonic Space is to bin the measured C_ℓ spectra in such a way to make the covariance matrix block-diagonal (e.g. Cabré et al. 2007). A simple rule of thumb discussed in Cabré et al. 2007 is to choose $\Delta\ell \, f_{sky} \sim 2$, which is in very nice agreement with the width of the $\text{Cov}(\ell, \ell')$ distribution in Fig. C1. It remains to be studied whether this have an impact in methods like BAO where one is after short-wavelength features on top of the broad band C_ℓ shape.